https://doi.org/10.5194/egusphere-2025-5327
Preprint. Discussion started: 23 December 2025

Untangling the effects of vertical mixing schemes and convective adjustment in the Mediterranean Sea

Lucia Gualtieri[1], Paolo Oddo[2], Hans Burchard[3], Federica Borile[2], Aimie Moulin[1], Pietro Miraglio[1], Francesco Maicu[1], Emanuela Clementi[1]

[1]CMCC Foundation - Euro-Mediterranean Center on Climate Change, Bologna, Italy.
[2]University of Bologna, Department of Physics and Astronomy, Bologna, Italy.
[3]Leibniz Institute for Baltic Sea Research Warnemünde, Rostock, Germany.

Correspondence to: Lucia Gualtieri (lucia.gualtieri@cmcc.it)

Abstract. The Mediterranean Sea provides a natural laboratory for investigating ocean circulation processes of global relevance due to its complex dynamics, active deep and intermediate water formation, and sensitivity to climate variability. Regional ocean circulation models skill strongly depends on the parameterization of subgrid-scale processes, among which turbulent vertical mixing and convection play a major role. To evaluate their impact in the context of the Mediterranean Sea two-year-long simulations were conducted using three vertical closure schemes – Richardson-number dependent parameterisation, Turbulent Kinetic Energy (TKE) scheme, and Generalised Length Scale (GLS) scheme – combined with a convective adjustment approach with the aim to study their interaction. Model results are evaluated against all available Argo floats data, both at the basin scale and in key deep and intermediate water formation regions. The simulations show that adding a convective adjustment is crucial to accurately reproduce observations with the Richardson-number dependent parameterization, where it improves all key variables, while for the TKE scheme it is particularly important for representing the mixed layer depth across the basin and in deep water formation areas. For more physics-based vertical schemes, like the GLS closure, the convective adjustment is mostly redundant and can occasionally degrade results. Overall, the GLS scheme without any convective adjustment provides the most accurate representation of the mixed layer depth as well as the vertical structure and variability both at basin scale and in key regions of deep and intermediate water formation.

1 Introduction

The Mediterranean Sea is a semi-enclosed basin characterized by intense thermohaline variability, strong mesoscale activity, and complex interactions with the atmosphere and surrounding land masses. Its dynamical features, including dense water formation, flux exchanges through narrow straits, and sub-basin circulations, make it a particularly challenging environment for ocean modeling (e.g., Pinardi and Masetti, 2000; Millot and Taupier-Letage, 2005; Testor et al., 2018). Despite its relatively small size, the Mediterranean Sea plays a crucial role in shaping the regional climate (e.g. Lionello et al., 2006; Pinardi and Masetti, 2000) and represents a natural laboratory for investigating key ocean processes with implications at the global scale. In this sense, it is often considered a “miniature ocean” (e.g., Bethoux et al., 1999), where processes such as deep and intermediate water formation, strait exchanges, mesoscale variability, and air–sea interactions can be studied in a confined environment as a small-scale analogue of global processes.

Over the past two decades, regional ocean models have been widely employed to simulate the Mediterranean circulation at increasing spatial and temporal resolution. Among these, the physical component of the Mediterranean Forecasting System, developed within the framework of the Copernicus Marine Service, represents a state-of-the-art implementation (e.g., Tonani et al, 2009; Clementi et al., 2017; Coppini et al., 2023). It provides regular, open-access analyses, forecasts (Clementi et al., 2023) and reanalyses (Escudier et al., 2021) of the basin's physical state and serves as a reference framework for scientific and operational applications.

Due to high computational costs and missing physics, the spatial and temporal resolution of current hydrostatic ocean circulation models, even at regional scale, is unable to explicitly resolve the inherently non-hydrostatic and small-scale turbulent vertical mixing and convective processes. To this end, vertical mixing closure schemes – either based on simplified formulations (e.g., Pacanowski and Philander, 1981) or on more physically based models (e.g., Gaspar et al., 1990; Umlauf and Burchard, 2003) – are employed to mimic these turbulent processes. Also, deep convection, which corresponds to the formation of dense deep water masses, has to be represented through parameterizations to reproduce its timing, intensity, and spatial extent realistically (e.g., Marshall et al., 1999; Villarreal et al., 2005; Herrmann et al., 2008; Luneva et al., 2019). Note that convection causes turbulent vertical mixing under unstably stratified conditions and can be parameterized separately (convective adjustment) or within the same turbulence closure scheme (Umlauf and Burchard, 2003; Legay et al., 2025).

The choice of mixing scheme and convective adjustment parameterisations has been shown to play a crucial role in shaping the circulation, the temperature and salinity distributions and deep water formation (DWF) processes (e.g., Herrmann et al., 2008; Reffray et al., 2015; Luneva et al., 2019; Robertson et al., 2019; Gutjahr et al., 2021). In particular, vertical mixing controls the redistribution of heat and salt throughout the water column, thereby influencing stratification and mixed layer depth (MLD). Convection, on the other hand, strongly affects deep and intermediate water formation, which in turn impacts large-scale circulation patterns and water mass properties. Since these processes are tightly coupled to air–sea exchanges and mesoscale dynamics, model sensitivity to the choice of mixing and convection schemes can propagate across a wide range of spatiotemporal scales, ultimately influencing the realism of simulated ocean variability.

Only a few previous studies provide a context for understanding the performance of different mixing schemes, but none of these explicitly investigate their combined effect with a convective adjustment. Madec et al. (1991) combined Richarson-number dependent closures with nonpenetrative convective adjustment in studies of deep water formation in the Northwestern Mediterranean Sea. Reffray et al. (2015) investigated the sensitivity of turbulent vertical mixing using a 1-D ocean circulation model at the global scale, comparing various mixing schemes but without including convective adjustment. Gutjahr et al.

https://doi.org/10.5194/egusphere-2025-5327
Preprint. Discussion started: 23 December 2025

(2021) compared various global-scale mixing schemes – including among the others, Richardson-number dependent closures and Turbulent Kinetic Energy (TKE) – but did not assess the role of convective adjustment. Storto et al. (2023) focused on the Mediterranean Sea, comparing the Generalized Length Scale (GLS) and TKE schemes, but did not examine cases of active convection and therefore did not evaluate the potential impact of including a convective adjustment. By explicitly investigating the interplay between vertical mixing schemes and convective adjustment, the present study addresses a gap left by these prior works and demonstrates how convective adjustment modulates the behaviour of different schemes in the context of the Mediterranean Sea.

The aim of this study is to investigate the sensitivity of a modified configuration of the Mediterranean Forecasting System (Clementi et al., 2023) to the choice of vertical mixing scheme and to the inclusion of an explicit convection adjustment parameterization. The experiments are performed using a 1/24° regional ocean model based on the Nucleus for European Modelling of the Ocean (NEMO; Madec et al., 2023, doi:10.5281/zenodo.6334656) coupled with the wind wave model WaveWatch III (WW3; Tolman et al., 2021), and forced by realistic atmospheric conditions over the two-year period 2020–2021. Three turbulence closure schemes are tested: the Richardson-number dependent parameterization (Pacanowski and Philander, 1981), the TKE closure scheme (Gaspar et al., 1990), and the GLS closure scheme (Umlauf and Burchard, 2003). These vertical mixing schemes are employed under two different convective setups: with and without the enhanced vertical diffusion parameterization typically used to mimic deep convection events. Model performance is evaluated across spatial and temporal scales through an intercomparison of temperature, salinity and mixed layer depth, from basin scale over years to deep and intermediate water formation regions ranging from months to hours.

The rest of the paper is structured as follows. Section 2 describes the region and the observational dataset used to assess our model performances. It also describes the model configuration, with a focus on the choice of the vertical mixing schemes and convective adjustment, and the experimental design performed in this study. Section 3 presents the main results of this study. We first present the convective adjustment (Subsection 3.1). Then we show results at the basin scale over the entire two-year period (Subsection 3.2). We focus then on deep and intermediate water formation regions over months to days (Subsection 3.3), and we investigate summer daily convection events at hourly temporal scales (subsection 3.4). Finally, Section 4 discusses the key conclusions and outlines perspectives for future work.

2 Data and methods

2.1 Argo float data in the Mediterranean Sea

Our model domain encompasses the entire Mediterranean Sea and extends into a portion of the Atlantic Ocean (Fig. 1a). Including an Atlantic box is essential to accurately resolve water exchanges between the Mediterranean Sea and the Atlantic Ocean through the Strait of Gibraltar, as the inflow of fresher Atlantic water and the outflow of saltier Mediterranean water strongly influence basin-wide salinity, temperature, and density structure, as well as deep water formation. Nevertheless, the analysis performed in this study focuses only on the Mediterranean Sea.

We use Argo float data (Wong et al., 2020; Poulain et al., 2007) from the Copernicus Marine Service Global Ocean near real-time in situ quality controlled observational product (Global Ocean-In-Situ Near-Real-Time Observations, https://doi.org/10.48670/moi-00036) as a reference observational dataset for our model validation. The location of Argo floats in the basin during the two-year period under investigation (2020–2021) is reported as red dots in Fig. 2a. Except for a few regions – such as the North Adriatic Sea, the Aegean Sea, the Strait of Sicily and the Gulf of Sirte – the Argo data in this time period provide good spatial coverage across the major part of the basin, offering a statistically meaningful dataset for our model validation.

Typical temperature and salinity profiles retrieved by Argo floats in the Mediterranean Sea are shown in Fig. 1 as monthly average vertical profiles of temperature and salinity in January 2021 (Fig. 1b) and July 2021 (Fig. 1c). The observations exhibit strong variability around the mean both in temperature and salinity, especially in the upper ~200 m, highlighted by shading representing one standard deviation of the dataset. It is known that, both temperature and salinity show also a pronounced seasonal variability (e.g., Pinardi and Masetti, 2000). In winter (Fig. 1b) stratification is weakened because of surface cooling and increased vertical mixing, resulting in the formation of a thick mixed layer with relatively uniform temperature and salinity. In summer (Fig. 1c), their values close to the surface become warmer and saltier as the result of strong heating and evaporation. These processes inhibit vertical mixing and give rise to a well-defined thermohaline stratification. As a result, vertical profiles are more homogeneous in winter and strongly stratified in summer.

https://doi.org/10.5194/egusphere-2025-5327
Preprint. Discussion started: 23 December 2025

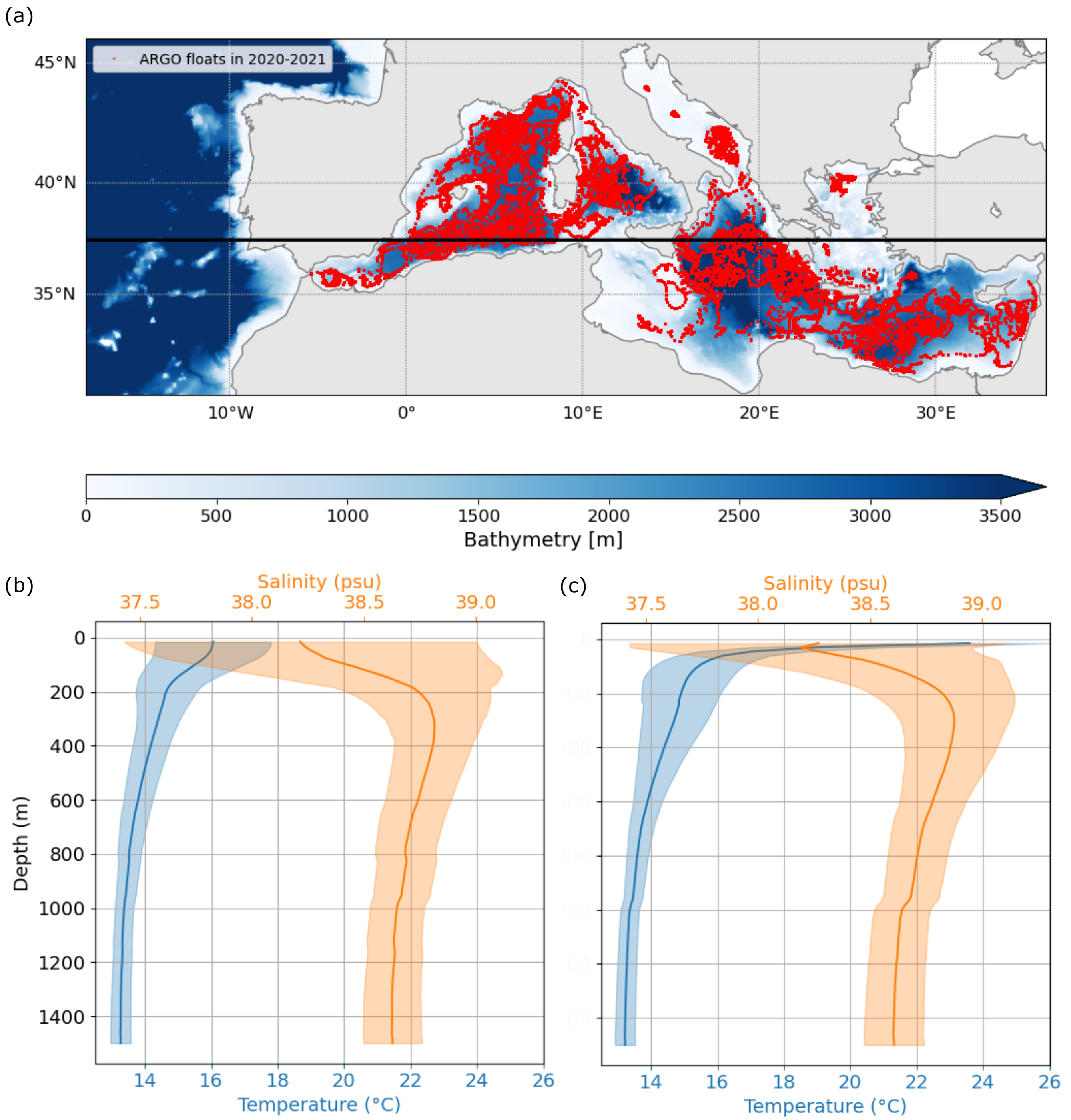

Figure 1: (a) Model domain including the Mediterranean Sea and an Atlantic box, with bathymetry as a background colour. Red dots indicate Argo floats during 2020–2021. The black zonal line at 37.5°N marks the location of a vertical section used throughout the paper. Bottom pannels show the basin-averaged observed temperature (blue) and salinity (orange) for (b) January 2021 and (c) July 2021, where shaded areas represent one standard deviation.

2.2 Model setup

The model system consists of a two-way coupled hydrodynamic circulation model and a third-generation spectral wind wave model. The ocean hydrodynamic circulation model is based on NEMO version 4.2 (Madec et al., 2023) and the wind wave model on WW3 version 6.07 (Tolman et al., 2021). The coupling happens hourly online with the exchange of air-sea temperature difference and surface currents from NEMO to WW3, and of neutral drag coefficient used to evaluate the surface wind stress from WW3 to NEMO (Clementi et al., 2017).

The model has a horizontal resolution of 1/24° (about 4 km) in both latitude and longitude, includes 141 non-uniformly distributed vertical levels, and uses a baroclinic time step of 180 s. The time stepping is achieved within a leapfrog differencing structure associated with an Asselin filter. The system is forced at the ocean surface with the atmospheric fields at 1/10° horizontal resolution of the European Centre for Medium-Range Weather Forecasts (ECMWF) made available by the Italian Air Force Meteorological Service. At the Atlantic boundary, the hydrodynamic model is nested into the daily analysis and forecast data of the Copernicus Marine Global product (Global Ocean Physics Analysis and Forecast, https://doi.org/10.48670/moi-00016) at 1/12° horizontal resolution and 50 vertical levels. River runoff in the modelling implementation originates from 39 rivers. Daily mean data for 38 of these rivers are taken from the European Flood Awareness System dataset (EFAS v5.0; Mazzetti et al., 2023) delivered within the Copernicus Emergency Service, while monthly mean data for the Nile River are taken from a climatology computed over the period 1970–2007 (Said et al., 2011). To capture the effects of intensified vertical mixing induced by internal wave breaking in the Strait of Gibraltar, particularly near Camarinal Sill (Wesson and Gregg, 1994; Hilt et al., 2020), we also prescribe an enhanced vertical diffusivity farther to the east of the sill.

Horizontal tracer advection is computed using the fourth-order Flux-Corrected Transport (FCT) scheme, which provides a good balance between accuracy and numerical stability by combining a high-order transport method with a monotonicity constraint (Gerbeau and LeRoux, 2001). Lateral diffusion of tracers is implemented as a Laplacian operator along isoneutral surfaces, with a spatially constant diffusivity. Horizontal momentum advection is treated in flux form using the third-order Upstream-Biased Scheme (UBS). As for tracers, momentum lateral diffusion is applied using a Laplacian operator along isoneutral surfaces, again with constant viscosity. These parameterisations are widely used in NEMO-based configurations for large-scale and regional ocean modelling, providing physically consistent dissipation while preserving the large-scale circulation features (e.g., Madec et al., 2023; Le Sommer et al., 2009).

2.2.1 Vertical mixing scheme

In this study, we compare three different parameterisations for vertical mixing, representative of the main families of vertical mixing parameterizations commonly used in ocean modelling. Our aim is to compare more simple approaches – such as the

Richardson-number dependent scheme, which is still used in the Mediterranean Forecasting system of the Copernicus Marine Service (Clementi et al., 2017; Coppini et al., 2023) – with more physically based formulations. The latter rely on a prognostic treatment of turbulence and are designed to capture a wider range of oceanic mixing processes with greater physical accuracy. Physically based vertical mixing schemes typically fall into two categories: one-equation and two-equation turbulence closure models. One-equation schemes solve a prognostic equation for the TKE while relying on diagnostic expressions or empirical assumptions for the mixing length or the dissipation rate (e.g., Gaspar et al., 1990). Two-equation models introduce an additional prognostic variable – usually the turbulence length scale or the dissipation rate of TKE – which allows for a more flexible and accurate representation of turbulence in stratified and sheared flows (e.g., Mellor and Yamada, 1982; Umlauf and Burchard, 2003). Each of these formulations requires calibrating several parameters. In this study, the best configuration for each scheme was selected from sensitivity tests as the one minimising statistical errors at the basin scale when compared with all available Argo data.

The first vertical mixing scheme used in this study is a Richardson number–dependent formulation originally proposed by Pacanowski and Philander (1981), where vertical eddy viscosity and diffusivity are parameterised as functions of the balance between stratification and vertical shear (see Appendix A). In this way, this scheme enhances mixing in regions of intense shear (or weak stratification) and reduces it under weak shear (or strong stratification). Specific parameters control the sensitivity of the mixing to these conditions, while background values ensure a minimum level of vertical mixing even under stable conditions. See Appendix B, Table B1, for details on the parameters used in the NEMO namelist for the Richardson number–dependent formulation.

The second vertical mixing scheme adopted here is the one-equation TKE scheme as proposed by Gaspar et al. (1990), in which the evolution of the turbulent kinetic energy k is described by a prognostic equation (see Appendix A). The model accounts for the main four physical processes involved in turbulence dynamics: production by vertical shear, destruction by buoyancy effects, turbulent kinetic energy diffusion, and dissipation parameterised following the Kolmogorov formulation (Kolmogorov, 1942). Vertical eddy viscosity A^{vm} is diagnosed from the TKE using a mixing length approach, where the mixing length is parametrized as a function of both a prescribed maximum and the local stratification to ensure numerical stability by limiting its vertical gradients. Tracer diffusivity $A^{vT} = A^{vS}$ for temperature and salinity, respectively, is derived from A^{vm} through a constant turbulent Prandtl number ($A^{vT} = A^{vm} / P_{rt}$). At the ocean surface, we impose a fixed minimum surface mixing length. A simplified representation of Langmuir turbulence is also included. See Appendix B, Table B2, for details on the parameters used in the NEMO namelist for the TKE closure scheme.

The third vertical mixing scheme used in this work is a two-equation turbulence closure scheme defined within the GLS framework (Umlauf and Burchard, 2003). The GLS schemes are a family of models that differ mainly in the choice of the second turbulence variable to be worked out through a prognostic equation and the stability functions used to parameterise stratification effects on turbulence. In addition to the turbulent kinetic energy *k*, the second prognostic variable can be defined in different ways, leading to different two-equation turbulence models. In the *k–ε* formulation, the second variable is the turbulent dissipation rate *ε*, which quantifies the rate at which turbulent kinetic energy is dissipated into heat. In the *k–ω* formulation, it is the specific dissipation rate $\omega = \epsilon/k$ (where ϵ represents the turbulent kinetic energy dissipation rate) which has the dimension of an inverse time and represents a characteristic turbulence frequency. Alternatively, in the *k–k*$_l$ formulation, the second variable is the turbulent length scale *k*$_l$, describing the typical size of the energy-containing eddies, usually expressed as $k_l \simeq \frac{k^{3/2}}{\epsilon}$.

In this study, we adopt the *k–ε* formulation, where the prognostic variables are the turbulent kinetic energy *k* and its dissipation rate *ε* (Umlauf and Burchard, 2003), but we also verified that using the *k–ω* formulation does not change significantly our conclusions. This model captures turbulence dynamics with enhanced detail, particularly under varying stratification, and is known for its numerical stability and robust performance in oceanic applications (Burchard and Bolding, 2001). The model prognoses the temporal evolution of *k* and *ε*, accounting for the same four physical processes considered in the TKE scheme: shear production, buoyancy destruction, vertical turbulent diffusion, and dissipation. Vertical eddy viscosity and diffusivity coefficients are computed dynamically based on *k* and *ε* and modulated by stability functions dependent on the gradient of the Richardson number. These stability functions, which are a common feature of turbulence closures, represent the suppression of turbulence by reducing mixing efficiency under stable stratification. In this study, we adopt the stability function formulation version A by Canuto et al., 2001 (*Canuto A*). Specifically, the momentum mixing efficiency decreases as stratification increases, while the turbulent Prandtl number correspondingly increases, implying a stronger reduction of tracer mixing relative to momentum (Canuto et al., 2001; Umlauf and Burchard, 2003). Boundary conditions at the surface and at the bottom incorporate enhancements to turbulence caused by wave breaking and bottom friction, respectively. Wave-induced mixing is not taken into account. More details on the GLS closure scheme are in Appendix A and the parameters used in the NEMO namelist are reported in Appendix B, Table B3.

2.2.2 Convective adjustment

Convective events are characterized by rapid and intense overturning of the water column, an inherent non-hydrostatic process that cannot be explicitly resolved by hydrostatic ocean models. As a result, convection must be represented through a dedicated parameterization. To better capture convective processes, it is still a common practice in large-scale modelling to apply a convective adjustment whenever the water column is statically unstable to mimic the rapid vertical homogenization associated with convective overturning and ensures realistic mixed layer deepening. One of the most common ways is to apply the enhanced vertical diffusivity (EVD) parameterisation (e.g., Lazar et al., 1999), widely adopted in ocean modelling (e.g., Large and Deleersnijder, 1993; Rahmstorf, 1993; Lazar et al., 1999; Griffies et al., 2000). In practice, the vertical eddy diffusivity coefficient is increased to a high constant value (typically between 1 and 100 $m^2 s^{-1}$) wherever the Brunt-Väisälä frequency squared N^2 becomes negative. In this study, a value of 10 $m^2 s^{-1}$ is prescribed for the vertical eddy diffusivity in these cases. Therefore, when the convective adjustment is applied, the vertical eddy diffusivity results from the combined effects of the vertical mixing closure schemes (whether the Richardson-number-dependent parameterization, the one-equation TKE scheme, or the two-equation GLS formulation) and the convective adjustment implemented through the EVD parameterisation. Since the TKE and GLS schemes implicitly include a convection parameterisation via the buoyancy term in the TKE equation (A3) and (A6) being positive for unstable stratification with N^2, some double counting is included in this approach. It should be noted that the GLS mixing parameterisation includes further sensitivity to convectively unstable stratification due to the dependence of the stability functions and the length-scale related equation on N^2.

2.3 Experimental design

We perform six, two-year long (2020–2021), simulations varying only the vertical mixing scheme and the inclusion or exclusion of convective adjustment. This experimental design allows us to assess the interplay between the choice of vertical mixing scheme and the effect of EVD, and to disentangle their individual and combined contributions to the representation of vertical mixing processes. It also enables us to evaluate how different turbulence closure schemes respond to the presence or absence of convective adjustment, and how this affects stratification, heat and salt distribution, and the overall vertical structure of the water column at basin and local scale.

Table 1 summarises the experiments. Our control run is defined as the simulation that employs the Richardson-number dependent vertical mixing scheme in combination with convective adjustment. Keeping convective adjustment active, we then replace the vertical mixing scheme with either TKE or GLS parameterisations. The remaining three experiments use the same three mixing schemes, but with convective adjustment disabled. In the experiments where convective adjustment is disabled, adaptive implicit vertical advection is activated to prevent local numerical instabilities (Shchepetkin, 2015, Madec et al., 2023). All simulations are initialized from the same 31 December 2019 restart fields provided by the Mediterranean Forecasting System.

Simulation name	Vertical mixing closure scheme	Convective adjustment	Notes
Exp-PP$^+$	Richardson-dependent scheme	Enhanced Vertical Diffusion (EVD)	Control simulation
Exp-TKE$^+$	Turbulent Kinetic Energy (TKE)	Enhanced Vertical Diffusion (EVD)	
Exp-GLS$^+$	Generalized Length Scale (GLS)	Enhanced Vertical Diffusion (EVD)	
Exp-PP	Richardson-dependent scheme	–	
Exp-TKE	Turbulent Kinetic Energy (TKE)	–	
Exp-GLS	Generalized Length Scale (GLS)	–	

Table 1: Summary of the experiments conducted in this study.

3. Results

3.1 Impact of the convective adjustment

The EVD parameterization exerts a strong control on the vertical structure of mixing. Figure 2 shows the eddy diffusivity coefficient along a zonal section at 37.5° N (as indicated in Fig. 2a) for different mixing configurations. The presence of convective adjustment together with different mixing schemes (Figs 2a, 2c, 2e) tends to mask the differences among the various vertical mixing parameterisations resulting in a very similar eddy diffusivity pattern regardless of the chosen vertical mixing scheme. Given the different eddy diffusivity scales observed in the experiments with and without EVD (Figs 2a, 2c, 2e *versus* Figs. 2b, 2d, 2f), it is clear that when EVD is active, the eddy diffusivity produced by the vertical mixing closure is largely overwritten by the EVD parameterization. In contrast, when convective adjustment is disabled (Figs. 2b, 2d, 2f), the vertical eddy diffusivity is determined solely by the mixing schemes and reveals more pronounced differences among schemes. Notably, the Richardson-dependent scheme (Figs. 2b) produces a relatively homogeneous increase in eddy diffusivity within the mixed layer, whereas the TKE (Figs. 2d) and GLS (Figs. 2f) schemes result in more heterogeneous structures. The magnitude of the vertical eddy diffusivity increases going from the Richardson-number dependent scheme (with maximum eddy diffusivity values on the order of 10^{-2} m^2/s) to the TKE and then to the GLS schemes (with maximum eddy diffusivity values on the order of 10^{-1} m^2/s). Moreover, when the EVD scheme is active, the maximum value of the vertical eddy diffusivity consistently occurs near the surface, while, when EVD is disabled, its maxima are typically found within the mid-depth of the mixed layer, which is more realistic due to the suppression of turbulent length at the top and the bottom of the mixed layer. This distinction underscores the role of EVD in favouring a surface-intensified mixing structure as opposed to the more symmetric and realistic profile observed in its absence, potentially impacting the MLD.

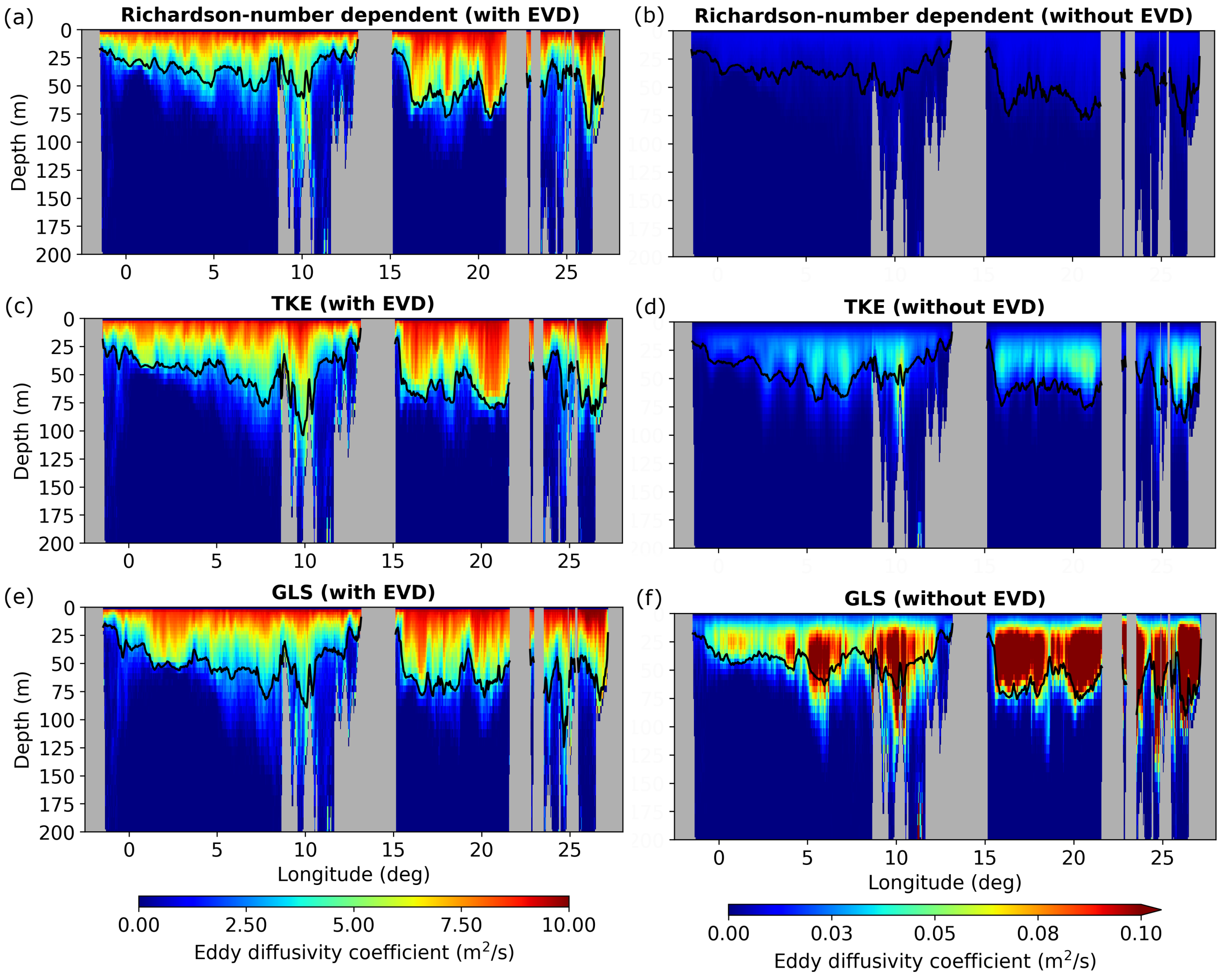

270 **Figure 2: Vertical eddy diffusivity coefficient along the zonal section at 37.5°N (black line in Fig. 1) averaged over January 2021 for different model configurations: (a) Richardson-dependent mixing scheme with EVD activated, and (b) without EVD activated; (c) TKE closure scheme with EVD activated, and (d) without EVD activated; (e) GLS scheme without EVD activated, and (f) with EVD activated. The black contours in each panel denote the depth of the mixed layer, while grey shading indicates land. Note the different eddy diffusivity scales for the experiments with and without EVD.**

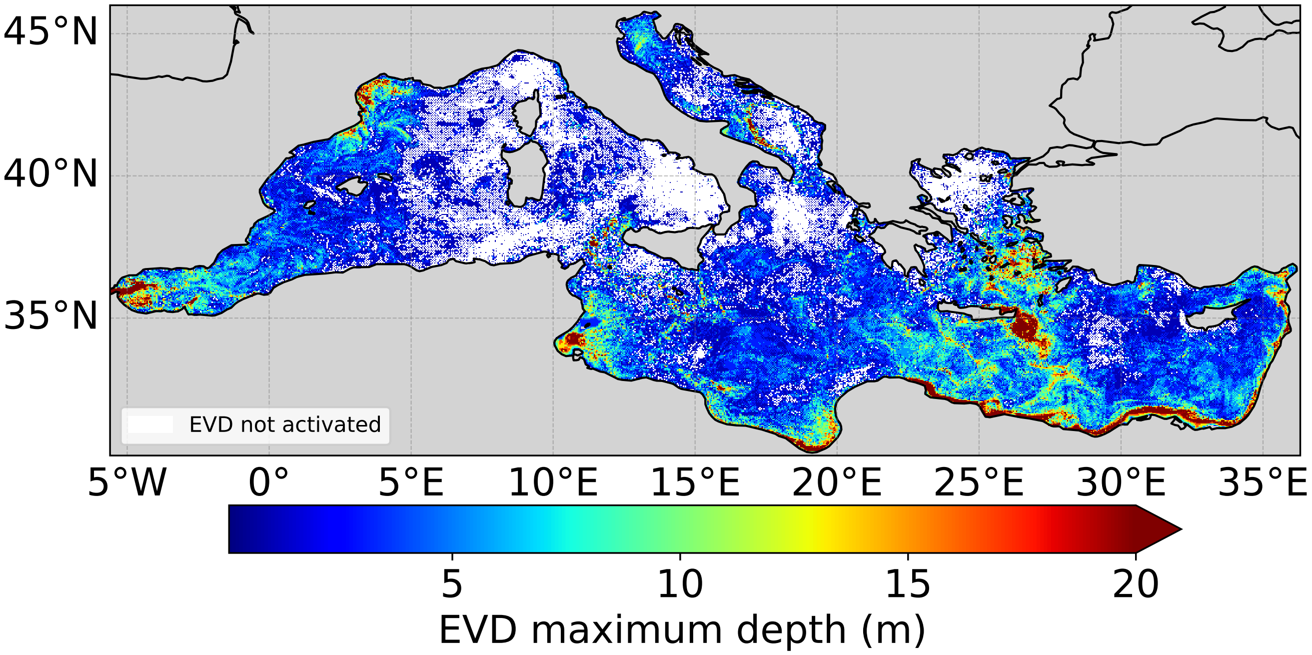

Figure 3: Map showing the maximum depth reached by the EVD parameterisation when activated in the control experiment (Exp-PP$^+$ in Table 1) during a summer day (1 July 2021). White areas indicate regions where EVD is inactive.

The EVD parameterisation is primarily intended to represent winter convection. However, convection-like vertical mixing occurs year-round, even outside the main winter season, and therefore the EVD parameterisation is active even in summer in some regions of the Mediterranean Sea. Figure 3 illustrates this by showing the maximum depth reached by the EVD on a summer day (1 July 2021) in the simulation using the Richardson-number dependent parameterization. White areas indicate the few regions where EVD is not applied on that day. Elsewhere the EVD is applied down to depths ranging from a few meters to several tens of meters reaching its maximum depth in the eastern Mediterranean Sea, and notably in the semi-permanent Ierapetra eddy region, located southeast of Crete. This activity is typically weaker and shallower than winter convection, but it still contributes to reshaping the vertical dynamics, as discussed in the following sections.

3.2 Assessment at the basin scale

3.2.1 Impact on tracers

Among the different experiments (Table 1), the simulation using the Richardson-number dependent vertical mixing scheme combined with a convective adjustment (Exp-PP$^+$) is taken as the control run. This configuration for the vertical mixing and convection corresponds to the current setup of the Mediterranean Forecasting System of the Copernicus Marine Service (Clementi et al., 2023).

To evaluate the performance of our control simulation and identify systematic deficiencies of the model, we compare the model outputs in terms of temperature and salinity with all available Argo data (Fig. 1a). Following the extensive literature on error decomposition for model validation (e.g., Willmott, 1981; Murphy, 1988; Murphy, 1992; Oke et al., 2002; Oddo et al., 2022), we define four key statistical metrics, which provide complementary insights into model skills: the root mean squared error (RMSE), the unbiased root mean squared error (uRMSE), the mean bias (MB), and the cross-correlation coefficient (CC). For more details on their definition, see Appendix C. We compute these four metrics averaging on the entire basin and over the entire two-year period.

The temperature error profiles are shown in Fig. 4. All metrics exhibit two pronounced decreases in model skill, one in the upper 50 m within the mixed layer and another between 200 and 600 m, corresponding to the Levantine Intermediate Waters (LIW) depth range (e.g., Bryden and Stommel:1982; Robinson and Golnaraghi, 1993; Theocharis et al., 2002). Within the mixed layer, RMSE and uRMSE peak at 25–30 m, corresponding to the yearly average MLD. MB reaches its maximum around the middle of the MLD (about 15 m). CC exhibits a monotonic reduced decrease throughout the mixed layer, with a minimum just below the yearly average MLD. A similar behaviour occurs within the LIW depth range, with a minimum in CC around 400 m, while RMSE, uRMSE and MB show their largest deviations slightly above, at approximately 350 m. Overall, this evidence indicates that errors are largest in the surface mixed layer but also reflect difficulties in representing intermediate water masses.

The salinity error profiles in Fig. 5 show a distinct pattern compared to temperature. RMSE and uRMSE exhibit a single peak confined to the mixed layer, with no significant anomalies at the LIW depth range. Nevertheless, the MB highlights systematic fresh biases at both depth ranges, suggesting persistent model errors in also salinity in representing the LIW. Like for temperature, the CC decreases monotonically within the mixed layer and shows only a weak secondary minimum at LIW depths. These findings suggest that salinity is overall less affected than temperature in the representation of intermediate waters, while it also presents a discrepancy with the observation within the mixed layer.

https://doi.org/10.5194/egusphere-2025-5327
Preprint. Discussion started: 23 December 2025

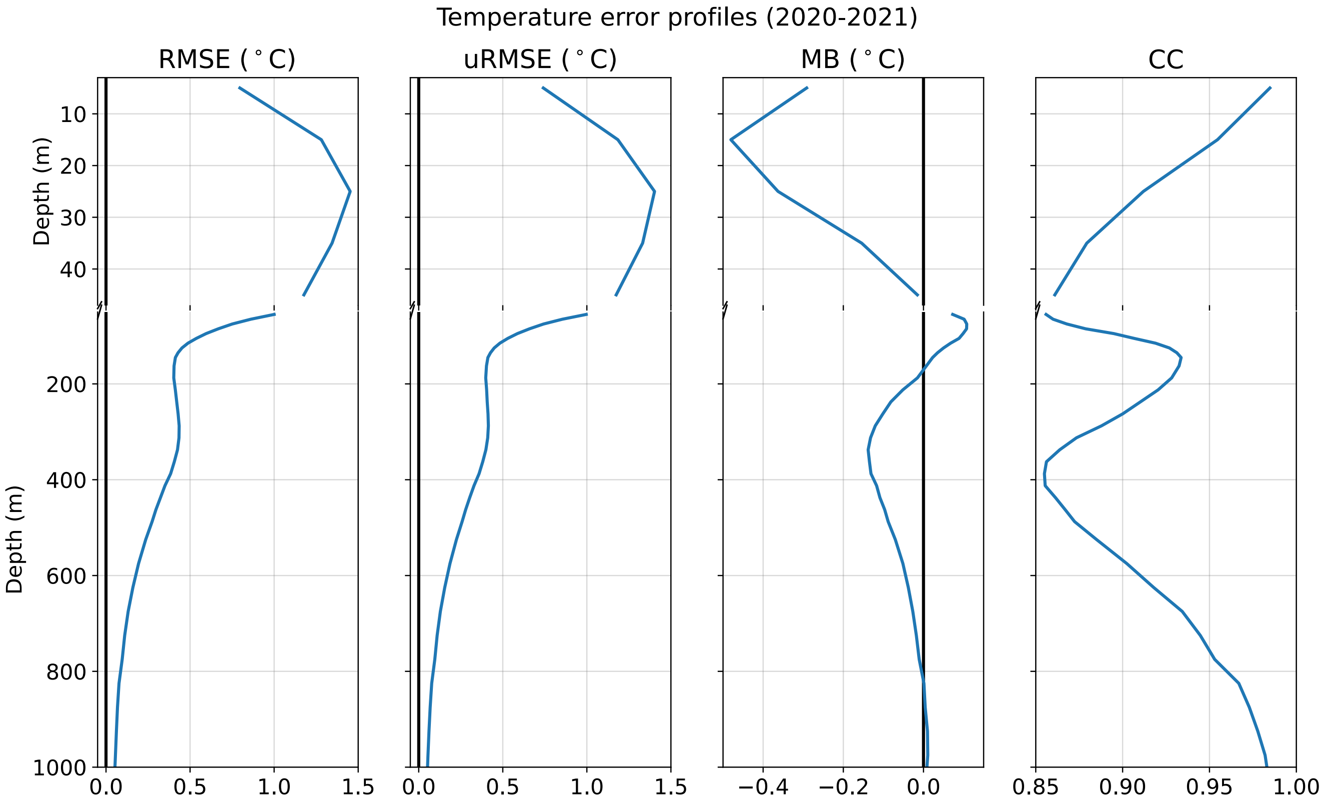

320 **Figure 4: Basin-averaged temperature error profiles for 2020–2021 in the control simulation (Exp-PP$^+$ in Table 1). Panels from left to right: root mean squared error (RMSE), unbiased root mean squared error (uRMSE), mean bias (MB), and cross-correlation coefficient (CC). The definitions of these metrices are in Appendix C.**

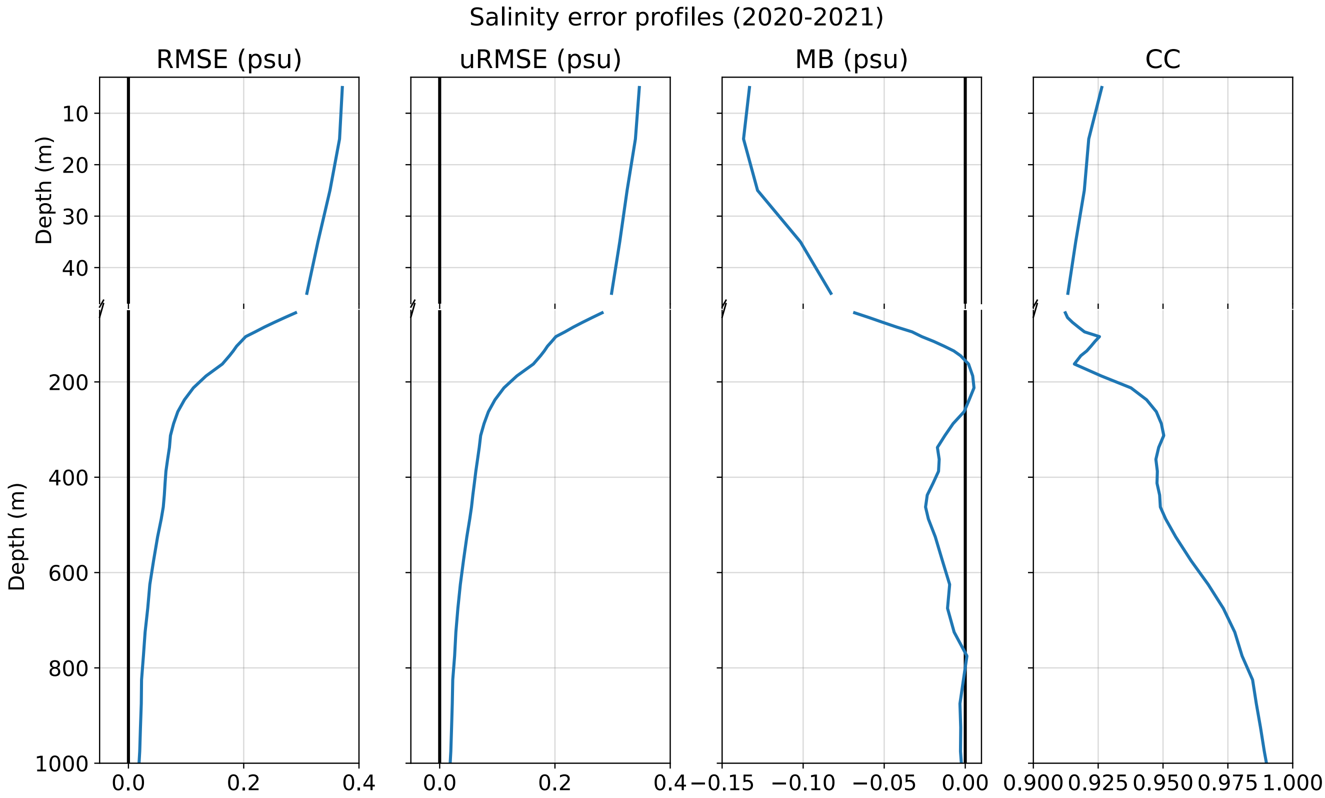

325 **Figure 5: Basin-averaged salinity error profiles for 2020–2021 in the control simulation (Exp-PP$^+$ in Table 1). Panels from left to right: root mean squared error (RMSE), unbiased root mean squared error (uRMSE), mean bias (MB), and cross-correlation coefficient (CC). The definitions of these metrices are in Appendix C.**

To assess the impact of the different closure schemes and the activation of the convective adjustment at the basin scale, we compare the metrices obtained for the other five simulations (simulation other than Exp-PP$^+$ in Tab. 1) with these of the control run. Figures 6 and 7 show the basin-averaged error difference for temperature and salinity, respectively. For each experiment and each metric (Equations C1–C4), the error difference (err_{diff}) as a function of depth is computed as

$$err_{diff} = err_{mod}(z) - err_{CS}(z) \quad (1)$$

where $err_{CS}(z)$ denotes the error of the control run (Exp-PP$^+$, see Figs. 4 and 5), and $err_{mod}(z)$ is the error associated with each model configuration (experiments other than Exp-PP$^+$ in Tab. 1). Here, err generically denotes one of the four metrics (RMSE, uRMSE, MB, or CC) detailed in Appendix C. For the MB metric, the absolute value of the mean bias is used for both the control run and the model experiments when computing err_{diff}.

It should be noted that negative values of RMSE, uRMSE, and MB indicate improvement, while positive values indicate deterioration. For CC, the interpretation is reversed: higher values (closer to 1) denote improvement, whereas lower values (towards 0) denote deterioration. Accordingly, in Figs. 6 and 7 green and red backgrounds highlight regions of improvement and deterioration relative to the control simulation respectively.

For temperature (Fig. 6), the RMSE indicates that the GLS closure scheme without convection parameterization (solid green line) provides the largest error reduction, a result further confirmed by the CC across all depths. The greatest improvement occurs within the mixed layer, mostly reflecting a reduction in systematic errors (MB), while additional improvements at LIW depths are observed in terms of uRMSE and CC. Adding the convection parameterization to GLS (dashed green line) diminishes these gains. The TKE mixing scheme exhibits intermediate skill: with or without EVD (orange lines), improvements are mostly confined to the mixed layer, while performance below this layer often deteriorates. The Richardson-dependent scheme without EVD (solid blue line) shows the largest degradation, consistent with the expectation that a closure scheme based solely on vertical shear and stratification requires additional parameterizations to represent properly convection.

For salinity (Fig. 7) in the absence of convective adjustment (solid lines), GLS is the only scheme showing improvements at some depths in RMSE, uRMSE and CC, and the smallest degradation in MB within the mixed layer. At the LIW depths, changes are minimal except for the configuration with GLS and EVD deactivated, which slightly improves RMSE, uRMSE and CC. The TKE and Richardson-number dependent schemes without EVD show deterioration across all metrics, particularly within the mixed layer, with the Richardson-number dependent scheme (solid blue line) performing worst, especially for MB.

https://doi.org/10.5194/egusphere-2025-5327
Preprint. Discussion started: 23 December 2025

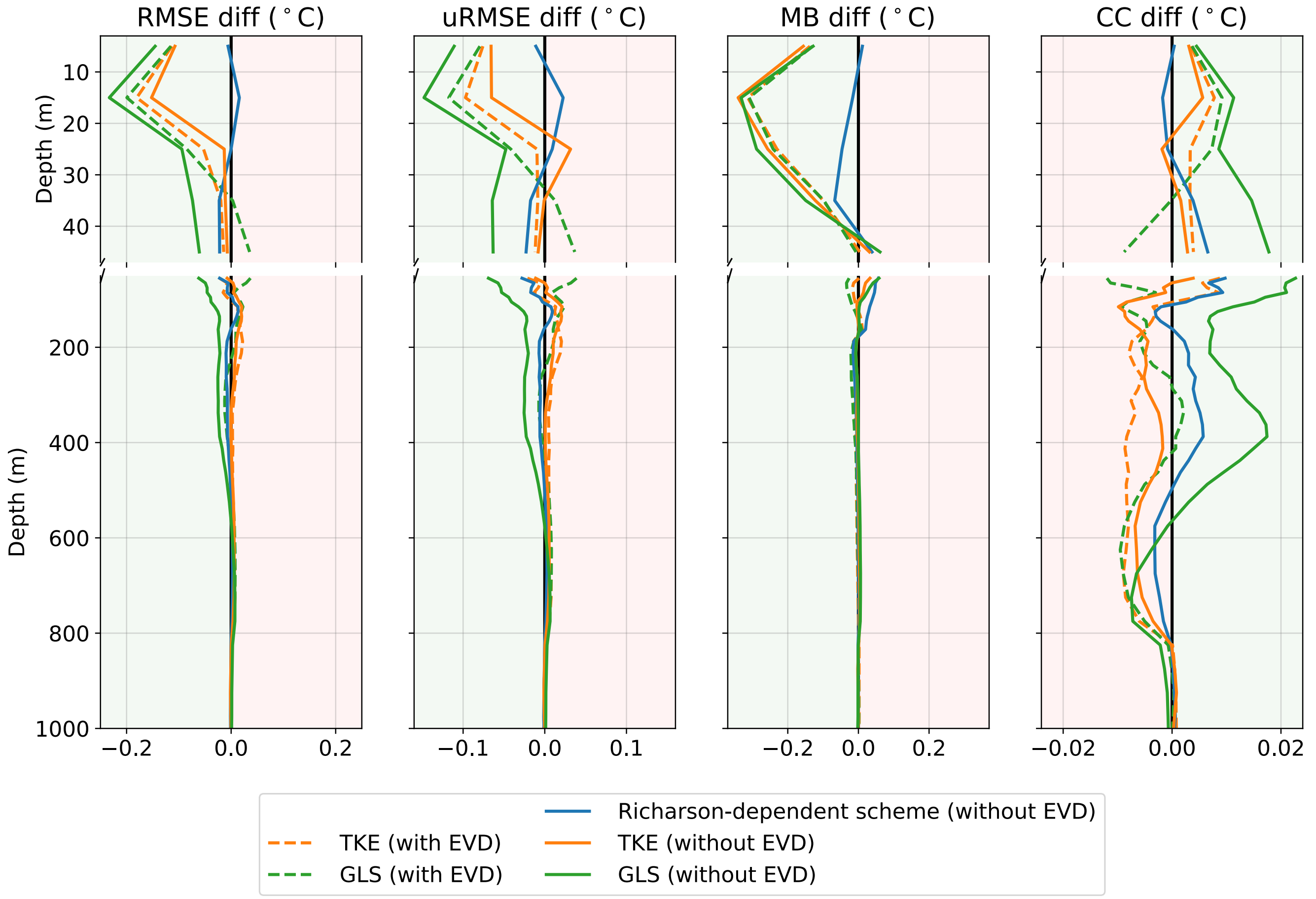

360

Figure 6: Temperature error difference (equation 1) with respect to the control simulation for the four metrics in equations C1–C4. Dashed lines indicate simulations with EVD and continuous lines without EVD. The transparent background color highlights regions of improvement (green) and worsening (red) compared to the control simulation.

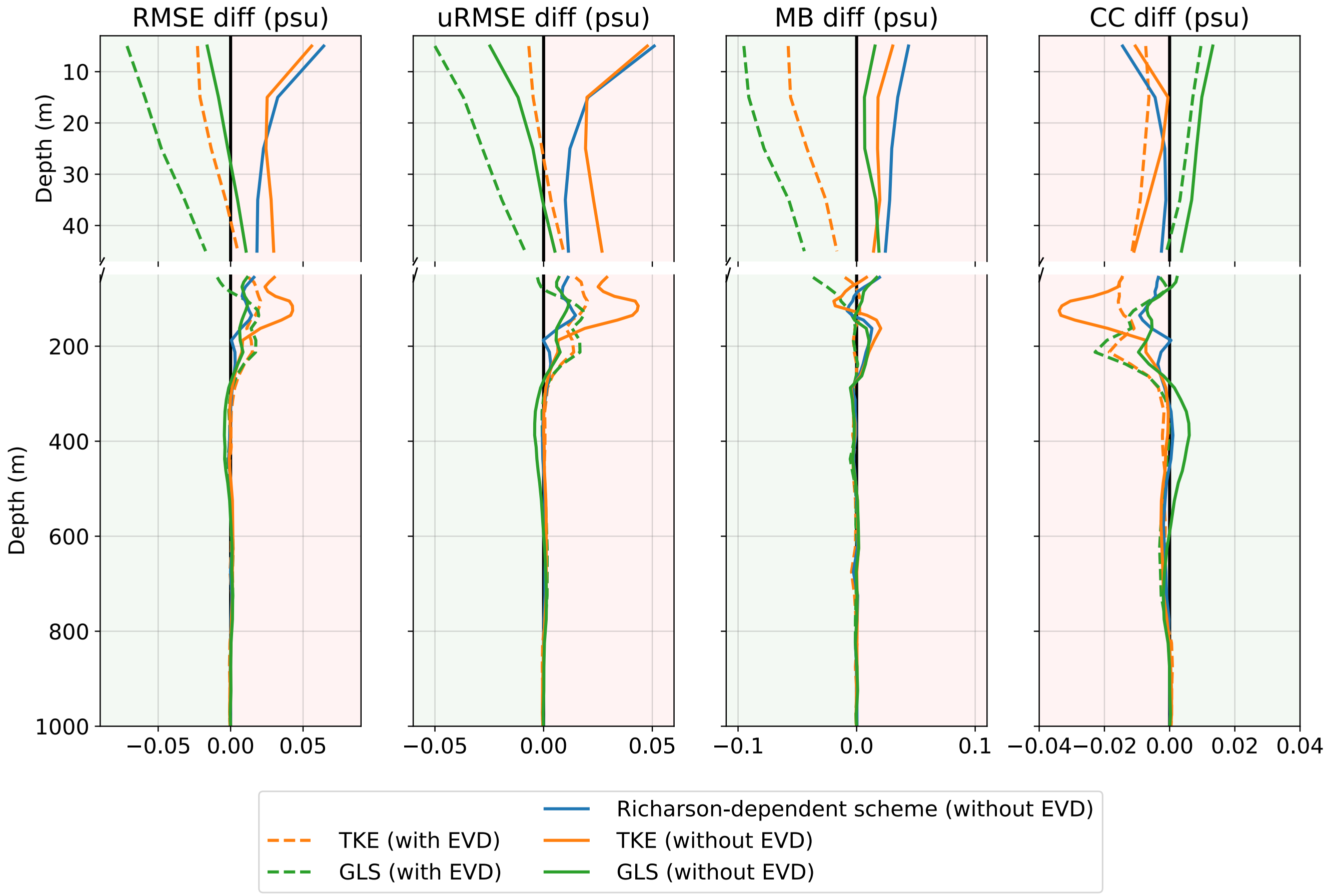

365

Figure 7: Salinity error difference (equation 1) with respect to the control simulation for the four metrics in equations C1–C4. Dashed lines indicate simulations with EVD and continuous lines without EVD. The transparent background colour highlights regions of improvement (green) and worsening (red) compared to the control simulation.

370 3.2.2 Representation of the Mixed Layer Depth

Given that the largest impact of the interplay between the mixing closure parameterisation and the convective adjustment occurs within the mixed layer, we also investigate how well the different schemes reproduce the MLD across the Mediterranean Sea. Figure 8 shows the time evolution of the MLD for the years 2020–2021, as computed from all available Argo temperature and salinity observations (black dashed line) and from model outputs (coloured lines) at the corresponding locations.

375

The MLD for both observations and model outputs is computed using the density threshold method, which identifies the depth at which the potential density increases by a fixed amount relative to a near-surface value. Specifically, here, the MLD is defined as the depth where the potential density exceeds that at 10 m by 0.01 kg m^{-3}. With this definition, a minimum MLD of

10 m is imposed, as the reference density is taken at that depth. This approach, commonly used in oceanographic studies, provides a robust estimate of the mixed layer under both stratified and convective conditions (e.g., de Boyer Montégut et al., 2004).

The temporal evolution of the basin-averaged MLD over the period 2020–2021 oscillates around a temporal-spatial average value of 31 m and exhibits a pronounced seasonal cycle, with deepening during winter and shoaling in summer. On average, the MLD reaches its maximum around 70–80 m in winter (December to March), when surface cooling and intense wind forcing promote vertical convection and deep mixing. In spring, the increasing solar radiation and weakening winds lead to rapid surface warming and stratification, resulting in a marked shoaling of the MLD. By summer (June to September), the MLD stabilises at its shallowest levels, below 20 meters, reflecting strong thermal stratification and limited vertical mixing. In autumn, cooling and more frequent wind events gradually deepen the MLD again, preparing the system for winter convection.

All simulations, colour-coded according to model configuration, reproduce this seasonal pattern, with winter maxima exceeding 70 m and summer minima around 15 m. However, significant differences in the MLD emerge while employing different vertical mixing schemes and varies also significantly depending on whether the EVD convection parameterisation is activated or not.

Simulations including EVD (blue, orange, and green lines) behave in a similar way and very close to the observations (black line). They occasionally show deeper (e.g. February–March 2020) or shallower (e.g. March 2021) winter MLDs and overall, they exhibit a good agreement in summer. With EVD activated, the two-year average MLD with TKE (31.1 m) and GLS (31.5 m) are very close to the observed one (31.0 m), while the Richardson-number dependent scheme tends to underestimate the MLD especially in summer (average of 28.4 m).

Simulations without EVD (red, purple, and brown lines) show distinct behaviours. The Richardson-dependent scheme (red line) produces the shallowest winter MLD and the lowest average MLD (average of 25.5 m), significantly underestimating observed deep mixing even in summer. The TKE scheme (purple line) tends to underestimate the MLD, both in winter and in summer. Although it performs better than the Richardson-number dependent scheme yet still fails to capture the basin-average maximum depths seen in observations (average MLD of 25.1 m). On the other hand, the GLS scheme (brown line) yields winter and summer MLDs closely aligned with observations, remaining in good agreement to them throughout the year. With the GLS, the average value of MLD without convective adjustment (31.7 m) is very close to the one obtained with convective adjustment included (31.5 m). This evidence demonstrates that this scheme does not need an additional external convection parameterisation to reproduce realistic mixed layer deepening.

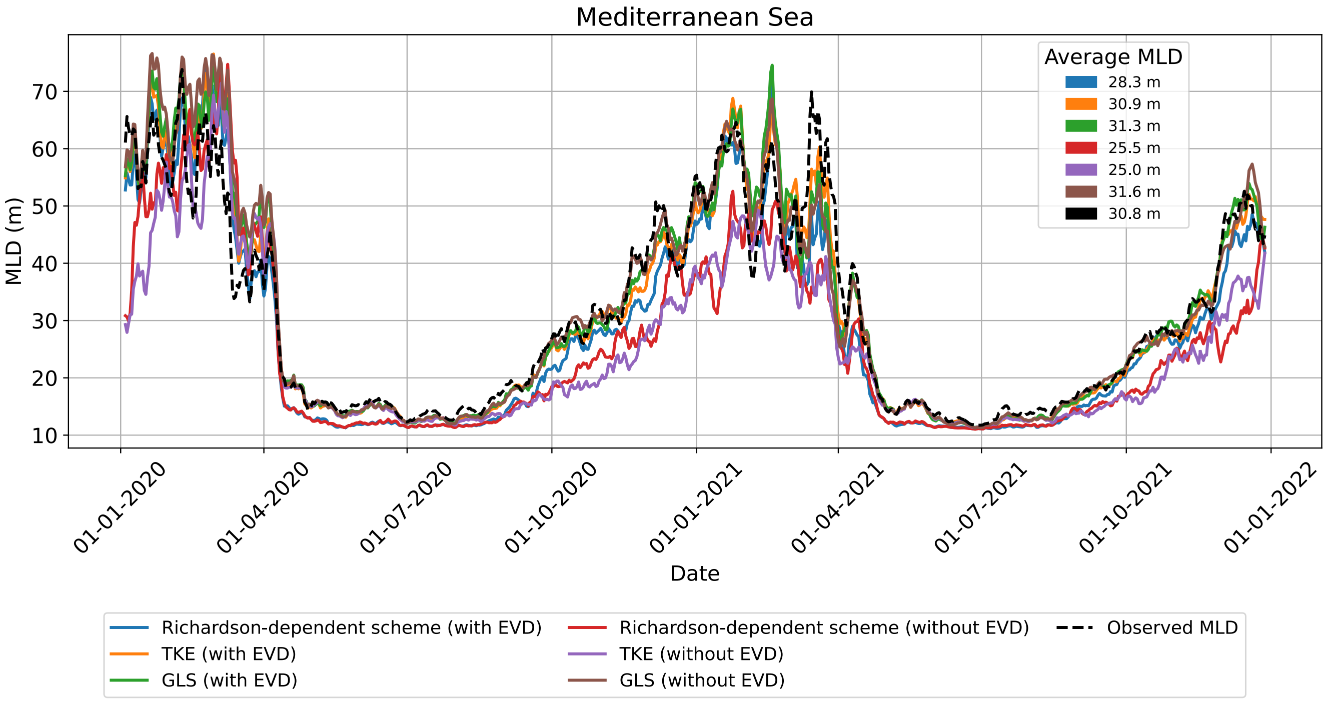

Figure 8: Time evolution of basin-averaged MLD for varying vertical mixing schemes, with and without convection parameterisation (configurations listed in Table 1). The black dashed line represents the MLD from Argo observations. A 7-day moving average has been applied to both model outputs and observations.

3.3 Assessment of water mass formation

The Mediterranean Sea hosts several key sites of deep and intermediate water formation, including the Gulf of Lion, the South Adriatic Sea, the Rhodes Gyre area and the Aegean Sea (e.g., Send et al., 1996; Lascaratos et al., 1999; Pinardi and Masetti, 2000; Pinardi et al., 2003; Pinardi et al., 2004, Pinardi et al., 2023). In these regions, vertical mixing and convection play a fundamental role in preconditioning and driving dense water formation processes by contributing to surface buoyancy loss and erosion of stratification (e.g., MEDOC group, 1970; Schroeder et al., 2012). The intensity and vertical structure of turbulent mixing directly influence the transformation and ventilation of water masses, making its accurate representation essential for modelling the basin-scale thermohaline circulation (e.g., Testor and Mortier, 2005; Somot et al., 2006; Simoncelli et al., 2022).

As case studies, to further investigate the impact of the interplay between different vertical mixing schemes and convective adjustment, we select one site of deep water formation and one site of both deep and intermediate water formation and analyse them across the various model configurations.

430 ### 3.3.1 Deep water formation in the south Adriatic Pit

The South Adriatic Pit (defined as in Simoncelli and Pinardi (2018) between longitudes 17°–19°E and latitudes 41°–42.5°N) is one of the principal sites of deep water formation in the Mediterranean Sea, where intense cooling and evaporation during winter – especially in February–March – induce strong density increases that drive dense water sinking and convective overturning (e.g., Lascaratos et al., 1999; Roether et al., 1996). During these events, the MLD can deepen substantially, typically reaching between 600 and 800 m (e.g., Lascaratos et al., 1999; Roether et al., 1996; Pinardi et al., 2023).

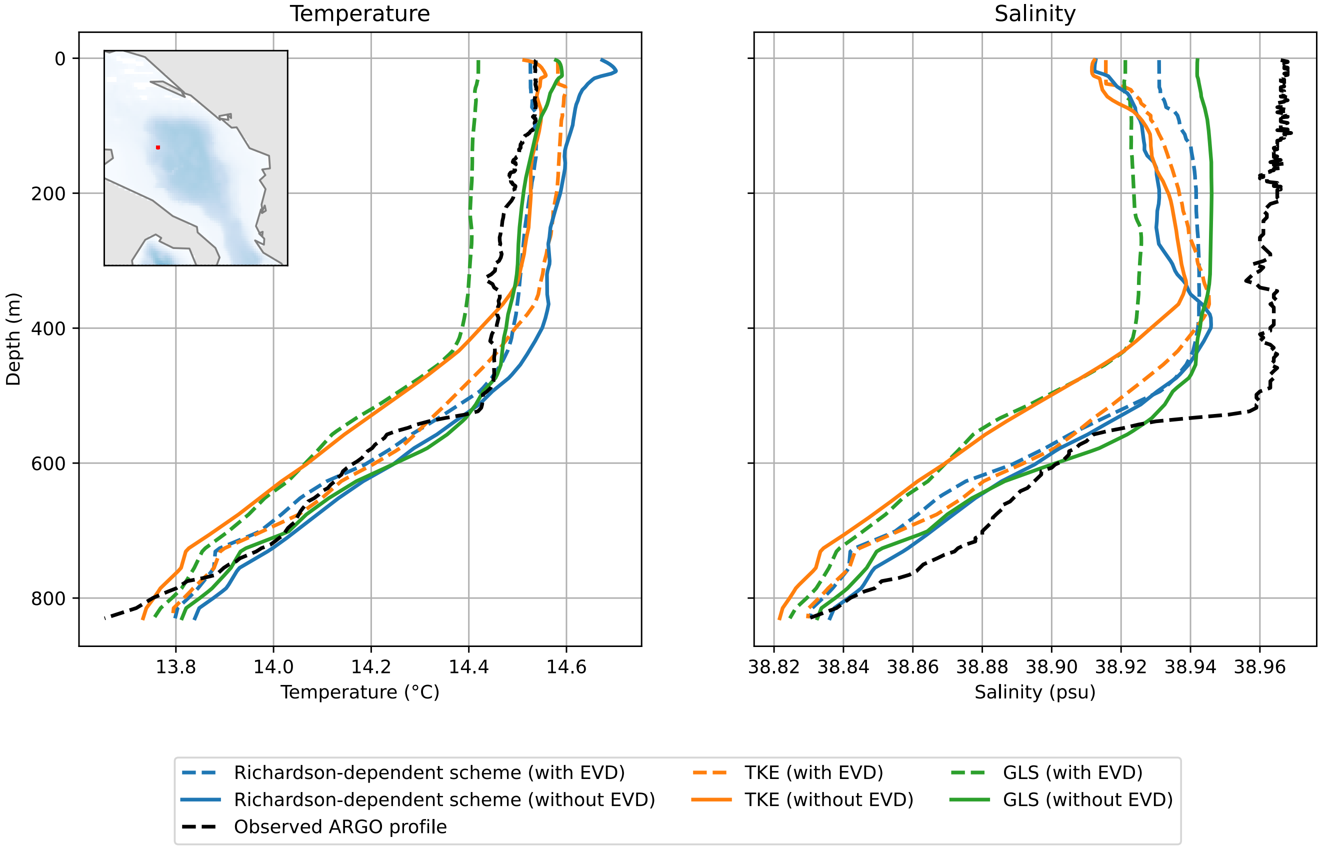

Figure 9: (a) Temperature and (b) salinity model profiles compared to observations (black dashed line) from an Argo float on 25 February 2021. Modelled profiles are color-coded by different vertical mixing schemes, with and without convective adjustment as indicated in the legend. The inset in the left panel shows the position of the Argo float.

In Fig. 9 we show the temperature and salinity profiles as recorded by an Argo float (black dashed line) on 25 February 2021 (location shown in the insert of Fig. 9a) in comparison with the modelled profiles at the same location for varying vertical mixing schemes and activating (dashed line) or deactivating (continuous line) the EVD. Argo data show a nearly uniform layer in the upper ~500 m, followed by a sharp gradient below. This inflection point corresponds to the MLD. Among the models in which EVD is active, the simplest Richardson-dependent scheme performs best, although it underestimates the MLD in the salinity profile of about 50 m. In this case, the GLS scheme underestimates the MLD in both temperature and salinity by about 100 m. In the absence of EVD, the situation is reversed. While the Richardson-dependent scheme underestimates the MLD and shows a reversed salinity gradient within the mixed layer, the GLS scheme captures the MLD depth well in both temperature and salinity, indicating that the GLS scheme performs better on its own, without convective adjustment. The TKE 450 scheme, both with and without EVD, underestimates the MLD by about 150 m and shows a reversed salinity gradient within the mixed layer.

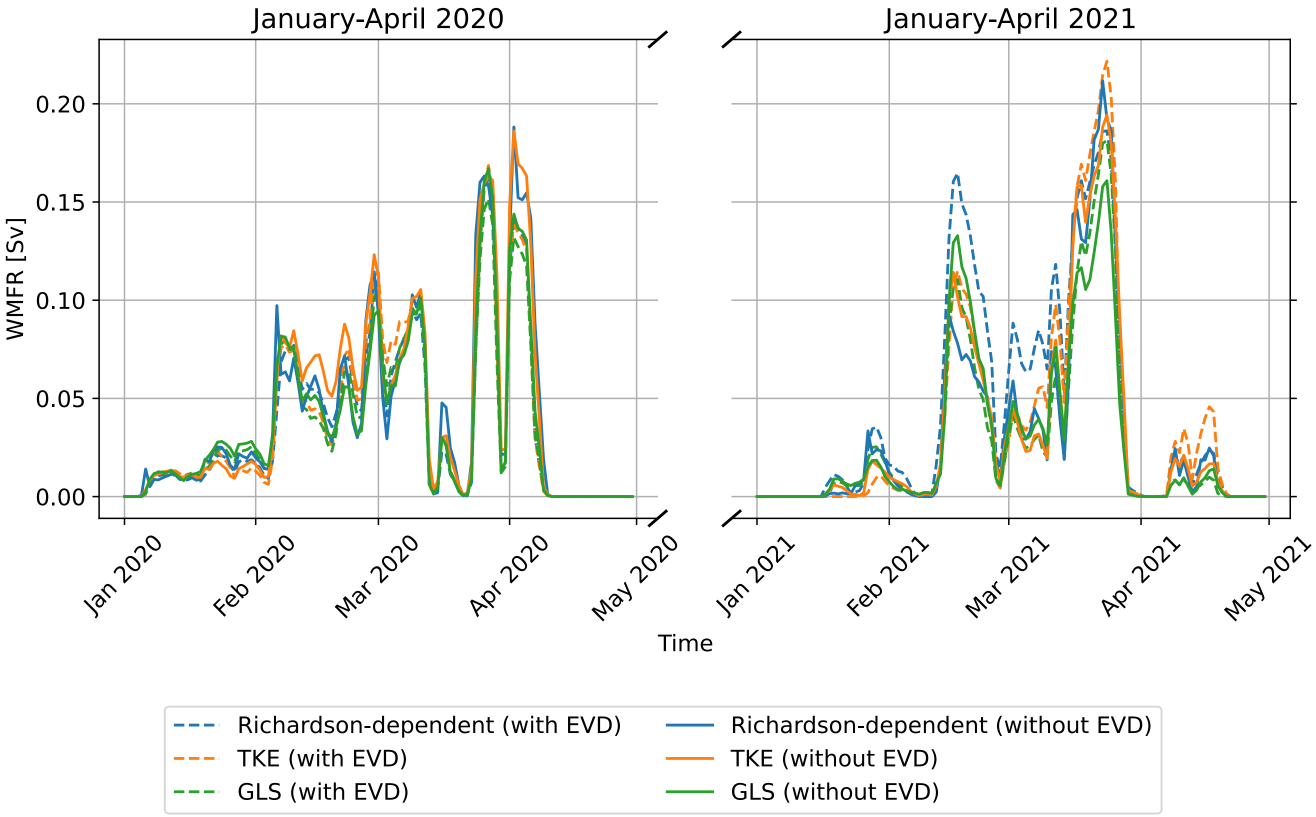

Figure 10: Daily water mass formation rate in the south Adriatic Pit. Curves are colour-coded by different vertical mixing schemes, 455 with and without convective adjustment as indicated in the legend.

To monitor the deep convection process in the South Adriatic Pit region we compute the water mass formation rate, following the criteria defined in Von Schuckmann et al. (2018), applied in Simoncelli and Pinardi (2018), and operationally computed yearly as Ocean Monitoring Indicator based on the Mediterranean Reanalysis system delivered within the Copernicus Marine Service. The water mass formation rate is defined as the volume of water above the mixed-layer depth with potential density 460 equal to or greater than 29.10 kg m^{-3}, divided by the number of seconds per year. Since this Ocean Monitoring Indicator is computed daily and very few observations per day are available in this small region, we calculate it using only modelled data for intercomparison. In Fig. 10 we show the water mass formation rate as computed for the six simulations with varying vertical mixing schemes and activation/deactivation of the convective adjustment, between January and April of each of the two years, that is the period over which deep water formation is expected in this region. We observe that in both years all models simulate a comparable amount of deep water, with only slightly larger inter–model differences in 2021. The largest discrepancy while activating or not the EVD occurs in February 2021 with the Richardson-number dependent scheme, while both TKE and GLS exhibit a comparable deep water formation rate.

3.3.2 Deep and intermediate water formation in the Rhode Gyre region

As an additional case study, we investigate the capability of the model to reproduce deep and intermediate water in the Rhodes Gyre region. This region, located in the eastern Mediterranean Sea between Rhodes and Cyprus, is where the Rhodes Gyre circulates and the Levantine Intermediate Water forms. This water mass, characterised by high salinity and intermediate depth (approximately 200–500 m), subsequently spreads across the Mediterranean Sea, influencing basin-scale thermohaline circulation (e.g., Kubin et al., 2019; Pinardi et al., 2023).

In Fig. 11a, we show the Hovmöller diagram of salinity data between January and April 2021 from all available Argo floats in the Rhodes Gyre region (defined as in Simoncelli and Pinardi (2018) between longitudes 26.3°–30°E and latitudes 34°–36.1°N). In Figs. 11b–11g we present the Hovmöller diagrams of MB (equation C3) of each model configuration with respect to the observations. All models show the largest errors between approximately 200 and 500 m, corresponding to the depth range of the LIW. We note that this error, originating in this region, spreads over time across the entire basin as shown in Section 3.2 and is clearly visible in the basin-averaged profiles in Figs. 4 and 5. Reducing this source of error in this region is therefore important for the entire Mediterranean Sea. In the presence of convective adjustment, among the configurations (Figs. 11b, 11d and 11f), the GLS closure scheme exhibits the largest errors, whereas without convective adjustment (Figs. 11c, 11e and 11g) the situation is reversed. While the Richardson-number dependent and the TKE schemes perform worse with EVD deactivated, the GLS scheme shows a significant improvement (average MB moves from 0.022 psu to 0.004 psu) demonstrating that while employing physics-based vertical mixing scheme the addition of external convective parameterization can deteriorate model results in this key region.

https://doi.org/10.5194/egusphere-2025-5327
Preprint. Discussion started: 23 December 2025

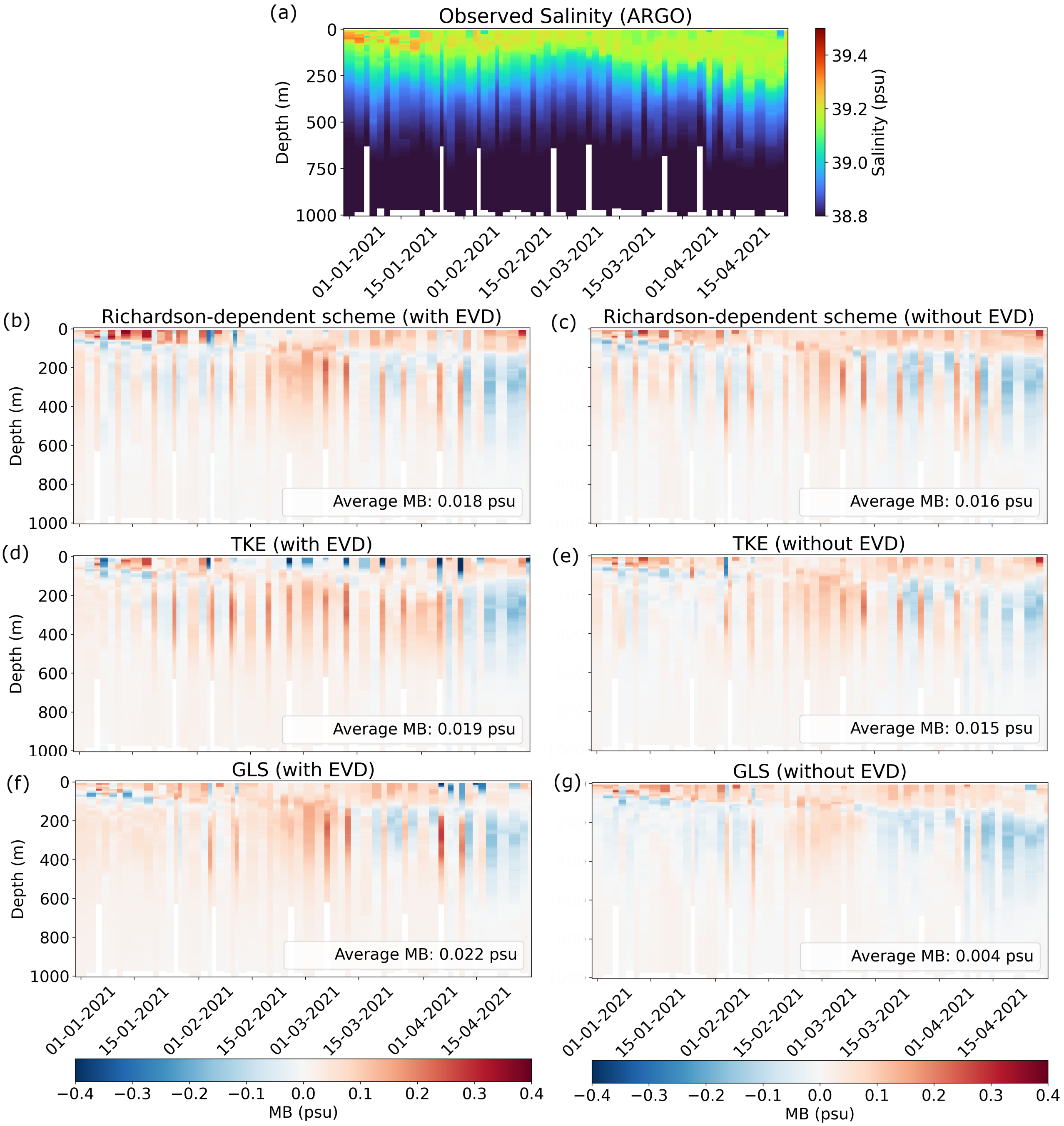

490 **Figure 11: (a) Hovmöller diagram of salinity data from available Argo floats in the Rhodes Gyre region between January and April 2021. (b–g) MB hovmöller diagrams of each model with respect to observations for different vertical mixing schemes and convective adjustment settings, as indicated in the title of each subfigure. The legend in each panel reports the average MB.**

https://doi.org/10.5194/egusphere-2025-5327
Preprint. Discussion started: 23 December 2025

3.4 Assessment of the nighttime summer convection daily cycle

In summer, the upper layers of the ocean exhibit a pronounced diurnal cycle in temperature, primarily controlled by the alternation of solar heating during the day and cooling processes at night. Surface waters warm under strong solar radiation, leading to a shallow, well-defined thermal stratification, while nocturnal cooling can erode this stratification. These processes occur within the mixed layer, which remains relatively shallow, as the rapid diurnal cycle of formation and destructing does not allow it sufficient time to deepen and night cooling is not as strong as in winter. Consequently, these processes are expected to be strongly influenced by the selected mixing scheme and the presence of a convective adjustment, which can significantly modify both the intensity of the heating and the depth of the near-surface warm layer. As shown in Fig. 3, the EVD during a summer day remains typically around an average of a few meters, but in certain areas – such as the Ierapetra semi-permanent gyre area within the Rhodes Gyre region as defined in the previous section – it can reach tens of meters.

The simulations in Tab. 1 were performed again starting from 1 July 2021 for three days, producing hourly outputs. The same initial conditions were used for all simulations, with the goal of monitoring how the mixing closure scheme and the presence of convective adjustment influence the daily cycle. As a case study, we focus on a site within the Rhodes Gyre region (27.5°E, 34.4°N) where the EVD reaches its greatest activation depth during summer (Fig. 3). Figure 12 shows the temperature profiles at that site for different days and times of the day.

The first profiles (lightest colours) show that at the beginning – on 1 July 2021, between midnight and 1 a.m. – the temperature profiles are well mixed and very similar to each other, with differences that are barely distinguishable, and are not yet influenced by the vertical mixing schemes or convective adjustment. Later the same day – between 6 p.m. and 7 p.m. – we observe that, while the simulations with TKE (orange) and GLS (green) behave in a similar way both with and without convective adjustment, the Richardson-number-dependent scheme (blue) is strongly influenced by it. In fact, in the case of TKE and GLS, the simulations without EVD (solid lines) produce temperature profiles that are only slightly different than those with EVD (dashed lines). By contrast, the Richardson-number dependent scheme without EVD (solid blue line) yields a nearly uniform temperature in the first 5 m, followed by a gradual decrease with depth. With EVD (dashed blue line) the profile is reversed, showing a surface and deep gradient separated by an intermediate quasi-homogeneous layer. In the following two days (2 and 3 July 2021, both at 6–7 p.m.) the difference between the Richardson-number dependent scheme and the other two schemes increases in both profile shape and amplitude, reaching a sea surface temperature (SST) difference larger than 0.5 °C on 3 July. Moreover, while the simulations with both TKE and GLS show only minor differences with and without EVD, those with the Richardson-number dependent scheme display much larger discrepancies, especially near the surface.

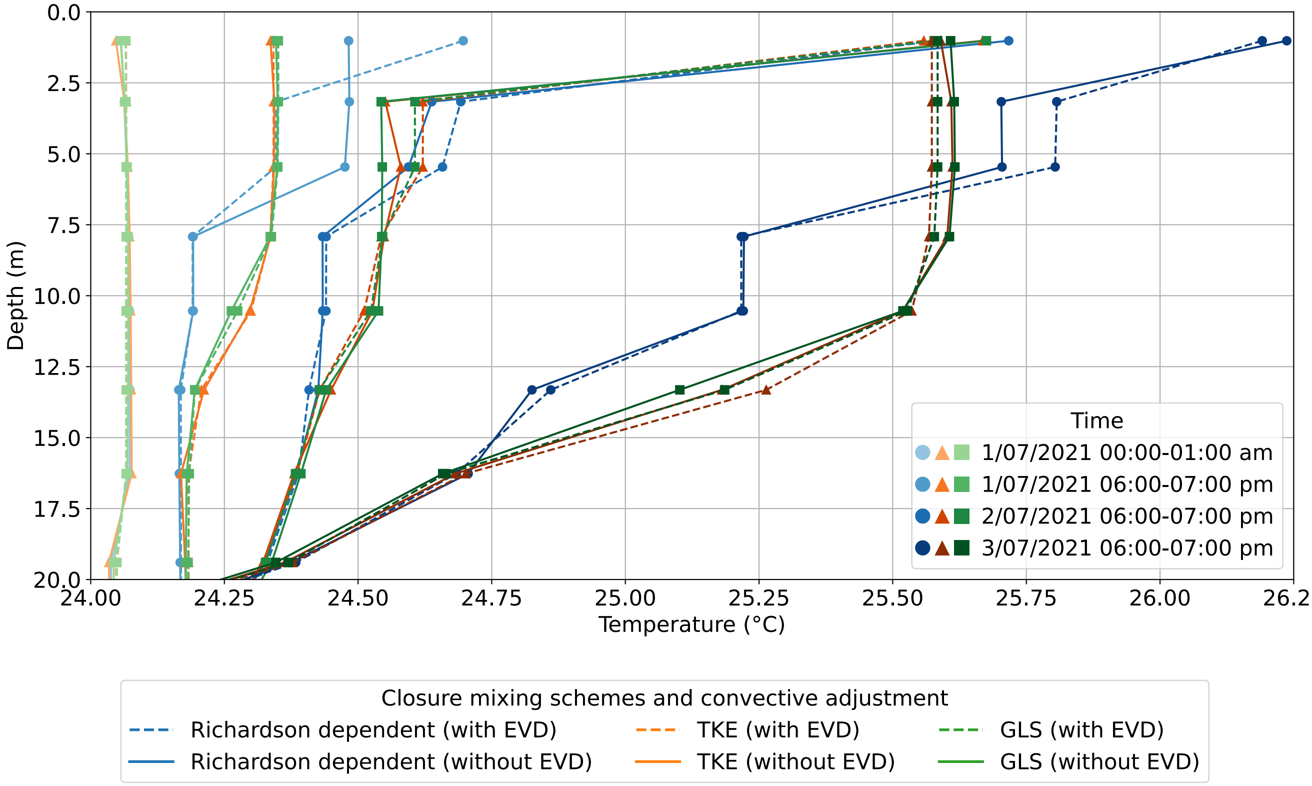

Figure 12: Temperature profiles at a site in the Rhodes Gyre area (27.5°E, 34.4°N) at different times of the day (see legend in the inset) and for different closure schemes and convective adjustment settings (see bottom legend).

4. Discussion and conclusions

In this work, we investigate how the interplay between different vertical mixing schemes – Richardson-number dependent scheme, TKE closure scheme, and GLS closure scheme – and an external convective adjustment affects the performance of a regional ocean circulation model of the Mediterranean Sea. The results first confirm what is known in the literature: the explicit representation of convection through enhanced vertical diffusion is crucial for simple schemes such as Richardson-number dependent closures. On the other hand, our results indicate that for more physically based schemes – such as the GLS closure scheme – which account for buoyancy loss in their equations, the convective adjustment may become redundant or even degrade the model's skill.

At the basin scale, our results show that the addition of a convective adjustment plays a different role depending on the mixing scheme. For the Richardson-number dependent scheme, EVD is crucial to accurately represent temperature, salinity and mixed layer depth. For the TKE closure scheme, it significantly improves the simulation of salinity and mixed layer depth, while for the GLS closure scheme, it provides some improvement for salinity but has little to no impact on temperature and mixed layer depth. Notably, the GLS scheme alone is able to reproduce the basin-scale seasonal variability of the MLD in good agreement with Argo observations, unlike the TKE scheme.

In deep water formation areas, such as the south Adriatic Pit, where convective processes play a central role during dense water formation events, we observe that the water mass formation rate is affected by the presence of EVD mainly when the mixing scheme is the simple Richardson-number dependent one. With TKE and GLS, a comparable amount of dense water is formed during the DWF season. Moreover, the MLD captured by Argo during DWF events is well reproduced only by the GLS without EVD, whereas its addition causes the MLD to be too shallow compared to observations. In areas of LIW formation, such as the Rhodes Gyre region, the representation of dense and salty waters improves significantly when using the GLS scheme without any external convective parameterization.

Focusing on nighttime convection during summer, analysed at an hourly timescale, we observe how the nighttime convective adjustment interacts with different vertical mixing schemes to shape the diurnal evolution of temperature. The EVD modifies the daily cycle and, consequently, the daytime temperature profiles mainly when using the Richardson-number dependent scheme; for the TKE and GLS schemes, it produces little change. Furthermore, temperature profiles using the Richardson-number dependent scheme differ noticeably from the other closure schemes, and after three days, the SST reaches a value roughly 0.5 ºC higher.

These findings underscore how critical it is, in regional ocean modelling, to align appropriately the mixing closure and convection parameterisations. More broadly, these results highlight that careful choice of a combination of subgrid-scale parameterizations is essential to reliably simulate key oceanographic features and improve model interpretability in regional applications. Future work could extend this analysis to longer-term simulations, the interaction with additional subgrid-scale processes – such as internal waves, eddy formation, and horizontal mixing – and to other semi-enclosed basins, in order to further improve model realism and predictive skill.

Appendix A

This appendix briefly summarizes the main equations of the three vertical mixing schemes used in this study, outlining how the eddy viscosity coefficient A^{vm} and diffusivity coefficient A^{vT} are determined for each scheme. We note that the eddy diffusivity coefficient for temperature, A^{vT}, is assumed to be equal to that for salinity: $A^{vS} \equiv A^{vT}$.

1. Richardson-number dependent mixing scheme

The first closure scheme used here is based on the Richardson number–dependent formulation originally proposed by Pacanowski and Philander (1981), where the vertical eddy viscosity and diffusivity are parametrized as

$$A^{vm} = \frac{A^{vm}_{ric}}{(1 + \alpha R_i)^n} + A^{vm}_b \quad \text{(A1)}$$

$$A^{vt} = \frac{A^{vm}}{(1 + \alpha R_i)} + A^{vT}_b \quad \text{(A2)}$$

Where $R_i = \frac{N^2}{(\partial U_h)^2}$ denotes the Richardson number, defined as the ratio between stratification (represented by the squared Brunt-Väisälä frequency, N^2) and vertical shear $(\partial U_h)^2$. The parameter A^{vm}_{ric} represents the maximum value of the eddy viscosity coefficient reached when $R_i < 0$; α and n are constant parameters. The additive terms $A^{vm}_b$and A^{vT}_b are background values that ensure a minimum level of vertical mixing even under stable conditions. For further details, see Pacanowski and Philander (1981) for the theoretical framework and Madec et al. (2023) for the practical implementation in NEMO.

2. **Turbulent Kinetic Energy (TKE) vertical mixing scheme**

The TKE vertical mixing scheme solves a prognostic equation for the turbulent kinetic energy k, while assuming a diagnostic closure for the tubulent length scale l_k. The TKE equation is written as

$$\frac{\partial k}{\partial t} = A^{vm} \left(\frac{\partial U_h}{\partial z}\right)^2 - A^{vT} N^2 + \frac{\partial}{\partial z}\left(A^{vm} \frac{\partial k}{\partial z}\right) - C_\epsilon \frac{k^{3/2}}{l_\epsilon} \quad \text{(A3)}$$

where U_h is the horizontal velocity, N^2 is squared Brunt-Väisälä frequency, C_ϵ is a constant and $l_\epsilon$is the dissipative length scale. On the right side of equation (A3), the four terms represent the main physical processes associated with vertical mixing. From left to right: shear production, stratification (or buoyancy) destruction, TKE diffusion and Kolmogorov dissipation (Kolmogorov, 1942). Vertical mixing coefficients are then computed as:

$$A^{vm} = C_k \, l_k \, \sqrt{k} \quad \text{(A4)}$$

$$A^{vT} = \frac{A^{vm}}{P_{rt}} \quad \text{(A5)}$$

where l_k is the mixing length scale, C_k is a model constant, and P_{rt} is the Prandtl number. The turbulent mixing length l_k is computed diagnostically and its value is constrained by stratification (typically $l_k = l_\epsilon = \sqrt{2k}/N$, with additional operational caps imposed). For further details, see Gaspar et al. (1990) for the theoretical framework and Madec et al. (2023) for the practical implementation in NEMO.

3. Generalized Length Scale (GLS) vertical mixing scheme

The GLS vertical mixing schemes solves two prognostic equations, one for the turbulent kinetic energy k and one for the generic length scale ψ. The evolution of the turbulent kinetic energy is governed by

$$\frac{\partial k}{\partial t} = \frac{A^{vm}}{\sigma_e}\left(\frac{\partial U_h}{\partial z}\right)^2 - A^{vT}N^2 + \frac{\partial}{\partial z}\left(A^{vm}\frac{\partial k}{\partial z}\right) - C_{0\mu}\frac{k^{3/2}}{l_\epsilon} \tag{A6}$$

The equation is coupled with a prognostic equation for the generic length scale:

$$\frac{\partial \psi}{\partial t} = \frac{\psi}{e}\left\{\frac{C_1 A^{vm}}{\sigma_\psi}\left(\frac{\partial U_h}{\partial z}\right)^2 - C_3\, A^{vT}N^2 - C_2 C_{0\mu}\frac{k^{3/2}}{l_\epsilon}F_{wall}\right\} + \frac{\partial}{\partial z}\left(A^{vm}\frac{\partial \psi}{\partial z}\right) \tag{A7}$$

Here, F_{wall} denotes the wall function and C_1, C_2, C_3, σ_k and σ_ψ are constants that depends on the choice of the turbulent model. $C_{0\mu}$ is also a constant. The wall function is only needed in the Mellor-Yamada model.

The eddy viscosity and diffusivity coefficients are then computed from the turbulent kinetic energy and mixing length:

$$A^{vm} = C_\mu\, l_k \sqrt{k} \tag{A8}$$

$$A^{vT} = C_{\mu'}\, l_k \sqrt{k} \tag{A9}$$

Where C_μ and $C_{\mu'}$ are the stability functions. The constant $C_{0\mu}$ depends on the choice of the stability functions. For further details, see Burchard and Bolding (2001) for the theoretical framework and Madec et al. (2023) for the practical implementation in NEMO.

https://doi.org/10.5194/egusphere-2025-5327
Preprint. Discussion started: 23 December 2025

Appendix B

In this appendix, we present the relevant portion of the namelist to be given as input to NEMO (version 4.2) corresponding to the three vertical mixing schemes used in this study. One table is provided for each scheme: Tabel B1 refers to the Richardson-number dependent schemes (Pacanowski and Philander, 1981), Table B2 to the TKE closure scheme (Gaspar et al., 1990) and Table B3 to the GLS closure scheme (Burchard and Bolding, 2001).

Parameter	Value	Explanation
rn_avm0	1.2e-6	vertical eddy viscosity [m2/s] (background value)
rn_avt0	1.0e-7	vertical eddy diffusivity [m2/s] (background value)
rn_avmri	100.e-4	maximum value of the vertical viscosity
rn_alp	5.0	coefficient of the parameterization
nn_ric	2	coefficient of the parameterization
ln_mldw	.false.	enhanced mixing in the Ekman layer

Table B1: Richardson-number dependent vertical mixing scheme

Parameter	Value	Explanation
rn_ediff	0.1	coefficient for vertical eddy diffusivity coefficient (avt=rn_ediff*mxl*sqrt(e))
rn_ediss	0.7	coefficient of the Kolmogoroff dissipation
rn_ebb	3.75	coefficient of the surface input of turbulent kinetic energy
rn_emin	1.e-8	minimum value of turbulent kinetic energy [m2/s2]
rn_emin0	5.e-4	surface minimum value of turbulent kinetic energy [m2/s2]
rn_bshear	1.e-20	background shear (>0) currently a numerical threshold (do not change it)
nn_pdl	1	Prandtl number function of Richarson number (=1, avt=pdl(Ri)*avm) or not (=0, avt=avm)
nn_mxl	2	mixing length: = 0 bounded by the distance to surface and bottom = 1 bounded by the local vertical scale factor = 2 first vertical derivative of mixing length bounded by 1 = 3 as =2 with distinct dissipative mixing length scale

ln_mxl0	.false.	mixing length scale surface value as a function of wind stress or not
rn_mxl0	0.04	surface buoyancy length scale minimum value
ln_mxhsw	.false.	mixing length scale surface value as a function of wave height or not
ln_lc	.true.	Langmuir cell parameterisation (Axell 2002)
rn_lc	0.15	coefficient associated to Langmuir cells
nn_etau	0	penetration of turbulent kinetic energy below the mixed layer (ML) = 0 none ; = 1 add a source of turbulent kinetic energy below the ML = 2 add a source of turbulent kinetic energy just at the base of the ML = 3 as = 1 applied on the high frequency part of the stress
nn_bc_surf	1	surface condition (0/1= Dirichlet/Neumann)
nn_bc_bot	1	bottom condition (0/1= Dirichlet/Neumann)

Table B2: Turbulent Kinetic Energy (TKE) vertical mixing schemes

Parameter	Value	Explanation
rn_emin	1.e-8	minimum value of turbulent kinetic energy [m2/s2]
rn_epsmin	1.e-12	minimum value of dissipation [m2/s3]
ln_length_lim	.true.	limit on the dissipation rate under stable stratification (Galperin et al., 1988)
rn_clim_galp	0.267	Galperin limit
ln_sigpsi	.true.	Activate or not Burchard (2001) modification for k-ε closure and wave breaking mixing
rn_crban	100	Craig and Banner (1994) constant for surface wave breaking mixing
rn_charn	70000	Charnock constant for wave breaking induced roughness length
rn_hsro	0.01	Minimum surface roughness
rn_hsri	0.03	Ice-ocean roughness
rn_frac_hs	0.4	Fraction of wave height as surface roughness
nn_z0_met	2	Method for surface roughness computation (0/1/2/3) = 0 constant roughness = 1 Charnock formula = 2 Roughness formulae according to Rascle et al., 2008 = 3 Roughness given by the wave model
nn_z0_ice	0	attenuation of surface wave breaking under ice

		= 0 no impact of ice cover = 1 roughness uses rn_hsri and is weigthed by 1-TANH(10*fr_i) = 2 roughness uses rn_hsri and is weighted by 1-fr_i = 3 roughness uses rn_hsri and is weighted by 1-MIN(1,4*fr_i)
nn_mxlice	0	mixing under sea ice = 0 No scaling under sea-ice = 1 scaling with constant Ice-ocean roughness (rn_hsri) = 2 scaling with mean sea-ice thickness = 3 scaling with max sea-ice thickness
nn_bc_surf	1	surface condition (0/1=Dirichlet/Neumann)
nn_bc_bot	1	bottom condition (0/1= Dirichlet/Neumann)
nn_stab_func	2	stability function (0=Galp, 1= KC94, 2=CanutoA, 3=CanutoB)
nn_clos	1	predefined closure type (0=MY82, 1=k-eps, 2=k-w, 3=Gen)

Table B3: Generalized Length Scale (GLS) vertical mixing scheme

Appendix C

Throughput this paper, we define four statistics metrics (e.g., Willmott, 1981; Murphy, 1988; Murphy, 1992; Oke et al., 2002, Oddo et al., 2022): the root mean squared error (RMSE), the unbiased root mean squared error (uRMSE), the mean bias (MB), and cross-correlation coefficient (CC). We denote $\bar{o}$ and $\bar{m}$ as the mean values of observations (o) and model data (m), N is the total number of observation-model pairs, and σ represents the standard deviation. The metrics are computed as follows:

- The root mean squared error (RMSE), which combines both systematic and random errors into a single measure of overall discrepancy:

$$RMSE = \sqrt{\frac{1}{N}\sum_{i=1}^{N}(m_i - o_i)^2} \tag{C1}$$

- The unbiased root mean squared error (uRMSE), which isolates the random component of the model error by removing the bias:

$$uRMSE = \sqrt{\frac{1}{N}\sum_{i=1}^{N}[(m_i - \bar{m}) - (o_i - \bar{o})]^2} \tag{C2}$$

- The mean bias (MB), which quantifies the average systematic difference between the model and observations:

$$MB = \bar{m} - \bar{o} \tag{C3}$$

- The cross-correlation coefficient (CC), which measures the degree of linear association between model outputs and observations:

$$CC = \frac{1}{\sigma_o}\frac{1}{\sigma_m}\frac{1}{N}\sum_{i=1}^{N}(m_i - \bar{m})(o_i - \bar{o}) \qquad (C4)$$

Code availability

The ocean hydrodynamic circulation model is based on the Nucleus for European Modelling of the Ocean (NEMO) version 4.2.0 (Madec et al., 2023), available on GitLab (https://forge.nemo-ocean.eu/nemo/nemo/-/releases/4.2.0) under doi:10.5281/zenodo.6334656. The wind-wave model is based on WAVEWATCH III^{TM} (WW3) version 6.07 (Tolman et al., 2021), accessible through GitHub (https://github.com/NOAA-EMC/WW3/releases). NEMO namelist configurations for the vertical mixing closure schemes used in this study are provided in Appendix B.

Author contribution

LG and PO conceived and designed the study with input from HB, who had a central role in the discussions and development strategy. LG implemented and tested the model setup through sensitivity experiments, with valuable contributions from FB and AM. LG performed the simulations and data analysis. PM contributed to the validation and visualization of the results. FM and EC participated in the discussions and provided feedback. LG wrote the manuscript with input and contributions from all authors, who reviewed and approved the final version of the manuscript.

Acknowledgements

The authors would like to thank Prof. Nadia Pinardi for insightful discussions throughout the development of this study and Prof. Paola Cessi for helpful comments.

References

Axell, L. B., Wind-driven internal waves and Langmuir circulations in a numerical ocean model of the southern Baltic Sea, Journal of Geophysical Research: Oceans, 107.C11, 25-1, 2002.

Bethoux, J. P., Gentili, B., Morin, P., Nicolas, E., Pierre, C., and Ruiz-Pino, D.: The Mediterranean Sea: a miniature ocean for climatic and environmental studies and a key for the climatic functioning of the North Atlantic, Progress in Oceanography, 44, 131–146, 1999.

Bryden, H. L. and Stommel, H.: The formation and circulation of deep water in the Mediterranean Sea, Nature, 296, 49–51, https://doi.org/10.1038/296049a0, 1982.

Burchard, H. and Bolding, K.: Comparative analysis of four second-moment turbulence closure models for the oceanic mixed layer, Journal of Physical Oceanography, 31, 1943–1968, https://doi.org/10.1175/1520-0485(2001)031<1943:CAOFSM>2.0.CO;2, 2001.

Burchard, H., Simulating the wave-enhanced layer under breaking surface waves with two-equation turbulence models, Journal of Physical Oceanography, 31, 11, 3133-3145, 2001.

Canuto, V. M., Howard, A., Cheng, Y., and Dubovikov, M. S.: Ocean turbulence. Part I: One-point closure model–momentum and heat vertical diffusivities, Journal of Physical Oceanography, 31, 1413–1426, https://doi.org/10.1175/1520-0485(2001)031<1413:OTPIOP>2.0.CO;2, 2001.

Clementi, E., Oddo, P., Drudi, M., Pinardi, N., Korres, G., and Grandi, A.: Coupling hydrodynamic and wave models: first step and sensitivity experiments in the Mediterranean Sea, Ocean Dynamics, 67, 1293–1312, 2017.

Clementi, E., Drudi, M., Aydogdu, A., Moulin, A., Grandi, A., Mariani, A., Goglio, A. C., Pistoia, J., Miraglio, P., Lecci, R., Palermo, F., Cop- pini, G., Masina, S., and Pinardi, N.: Mediterranean Sea Physical Analysis and Forecast (CMEMS MED-Physics, EAS8 system)(Version 1)[Data set], https://doi.org/10.25423/CMCC/MEDSEA_ANALYSISFORECAST_PHY_006_013_EAS8, 2023.

Coppini, G., Clementi, E., Cossarini, G., Salon, S., Korres, G., Ravdas, M., Lecci, R., Pistoia, J., Goglio, A. C., Drudi, M., et al.: The mediterranean forecasting system–part 1: evolution and performance, Ocean Science, 19, 1483–1516, 2023.

Craig, P. D., and Banner, M.L., Modeling wave-enhanced turbulence in the ocean surface layer, Journal of Physical Oceanography, 24, 12, 2546-2559, 1994.

de Boyer Montégut, C., Madec, G., Fischer, A. S., Lazar, A., and Iudicone, D.: Mixed layer depth over the global ocean: An examination of profile data and a profile-based climatology, Journal of Geophysical Research: Oceans, 109, C12003, https://doi.org/10.1029/2004JC002378, 2004.

Drévillon, M., Bourdallé-Badie, R., Derval, C., Lellouche, J., Rémy, E., Tranchant, B., Benkiran, M., Greiner, E., Guinehut, S., Verbrugge, N., Garric, G., Testut, C.-E., Laborie, M., Nouel, L., Bahurel, P., Bricaud, C., Crosnier, L., Dombrowsky, E., Durand, E., Ferry, N., Hernandez, F., Le Galloudec, O., Messal, F., and Parent, L.: The GODAE/Mercator-Ocean global ocean forecasting system: results, applications and prospects, Journal of Operational Oceanography, 1, 51–57, https://doi.org/10.1080/1755876X.2008.11020095, 2008.

Escudier, R., Clementi, E., Omar, M., Cipollone, A., Pistoia, J., Aydogdu, A., Drudi, M., Grandi, A., Lyubartsev, V., Lecci, R., Cretí, S., Masina, S., Coppini, G., and Pinardi, N.: A High Resolution Reanalysis for the Mediterranean Sea, Frontiers in Earth Science, 9, 1060, https://doi.org/10.3389/feart.2021.702285, 2021.

Galperin, B., Kantha, L. H., Rosati, A., & Hassid, S., A quasi-equilibrium turbulent energy model for geophysical flows, Journal of the atmospheric sciences, 45(1), 55-62, 1988.

Gaspar, P., Grégoris, Y., and Lefevre, J. M.: A simple eddy kinetic energy model for simulations of the oceanic vertical mixing: Tests at station Papa and long-term upper ocean study site, Journal of Geophysical Research: Oceans, 95, 16179–16193, https://doi.org/10.1029/JC095iC09p16179, 1990.

Gerbeau, J.-F. and Le Roux, A.: A flux-based method for convection-diffusion equations in ocean modelling, Ocean Modelling, 3, 229–239, https://doi.org/10.1016/S1463-5003(01)00006-2, 2001.

Global Ocean Physics Analysis and Forecast. E.U. Copernicus Marine Service Information (CMEMS). Marine Data Store (MDS). doi: https://doi.org/10.48670/moi-00016 (Accessed on 28-10-2025)

Global Ocean-In-Situ Near-Real-Time Observations. E.U. Copernicus Marine Service Information (CMEMS). Marine Data Store (MDS). doi: https://doi.org/10.48670/moi-00036 (Accessed on 28-10-2025)

Griffies, S. M., Bryan, K., Gnanadesikan, A., Hallberg, R. W., Marshall, J., and Samuels, B. L.: Developments in ocean climate modeling, Ocean Modelling, 2, 123–192, https://doi.org/10.1016/S1463-5003(00)00014-7, 2000.

Gutjahr, O., Brüggemann, N., Haak, H., Jungclaus, J. H., Putrasahan, D. A., Lohmann, K., and von Storch, J.-S.: Comparison of ocean vertical mixing schemes in the Max Planck Institute Earth System Model (MPI-ESM1. 2), Geoscientific Model Development, 14, 2317– 2349, 2021.

Herrmann, M., Somot, S., Sevault, F., Estournel, C., and Déqué, M.: Modeling the deep convection in the northwestern Mediterranean Sea using an eddy-permitting and an eddy-resolving model: Case study of winter 1986–1987, Journal of Geophysical Research: Oceans, 113, 2008.

Hilt, M., Roblou, L., Nguyen, C., Marchesiello, P., Lemarié, F., Jullien, S., Dumas, F., Debreu, L., Capet, X., Bordois, L., Benshila, R., and Auclair, F.: Numerical modeling of hydraulic control, solitary waves and primary instabilities in the Strait of Gibraltar, Ocean Modelling, 151, 101 642, https://doi.org/10.1016/j.ocemod.2020.101642, 2020.

Kolmogorov, A. N.: Equations of turbulent motion in an incompressible fluid, Izvestiya Akademiya Nauk SSSR, Seriya Fizicheskaya, 6, 56–58, 1942.

Kubin, E., Poulain, P.-M., Mauri, E., Menna, M., and Notarstefano, G.: Levantine Intermediate and Levantine Deep Water Formation: An Argo Float Study from 2001 to 2017, Water, 11, 1781, https://doi.org/10.3390/w11091781, 2019.

Large, W. G. and Deleersnijder, E.: Stability functions for a mixed-layer model, Journal of Physical Oceanography, 23, 778–785, https://doi.org/10.1175/1520-0485(1993)023<0778:SFFAML>2.0.CO;2, 1993.

Lascaratos, A., Brenner, L., Candela, N., Goy, J.-F., and Robinson, A. R.: Mediterranean Deep Water Formation: A Review, Progress in Oceanography, 44, 5–36, https://doi.org/10.1016/S0079-6611(99)00018-3, 1999.

Lazar, A., Madec, G., and Delecluse, P.: The deep interior downwelling, the Veronis effect, and mesoscale tracer transport parameterizations in an OGCM, Journal of physical oceanography, 29, 2945–2961, 1999.

Legay, A., B. Deremble, H. Burchard, Derivation and implementation of a non-gradient term to improve the oceanic convection representation within the k-ε parameterization, J. Adv. Model. Earth Syst., 17, e2024MS004243, 2025. https://doi.org/10.1029/2024MS004243

Le Sommer, J., Penduff, T., Madec, G., Jourdain, N. C., Beckmann, A., and Barnier, B.: Modeling the dynamics of the mesoscale eddy field in the North Atlantic ocean: Scale selection and parameter sensitivity, Journal of Climate, 22, 3017–3039, https://doi.org/10.1175/2008JCLI5714.1, 2009.

Lionello, P., Malanotte-Rizzoli, P., Boscolo, R., (eds). *Mediterranean climate variability*, vol. 4. Elsevier, 2006.

Luneva, M., Wakelin, S., Holt, J., et al.: Challenging Vertical Turbulence Mixing Schemes in a Tidally Energetic Environment: 1. 3-D Shelf-Sea Model Assessment, Journal of Geophysical Research: Oceans, 124, 6360–6387, https://doi.org/10.1029/2018JC014307, 2019.

Madec, G. and the NEMO System Team: NEMO Ocean Engine Reference Manual, Tech. rep., https://doi.org/10.5281/zenodo.8167700, 2023.

Madec, G., Delecluse, P., Crepon, M., and Chartier, M.: A three-dimensional numerical study of deep-water formation in the northwestern Mediterranean Sea, Journal of Physical Oceanography, 21, 1349–1371, 1991.

Marshall, J. and Schott, F.: Open-ocean convection: Observations, theory, and models, Reviews of Geophysics, 37, 1–64, https://doi.org/10.1029/98RG02739, 1999.

Mazzetti, C., Carton De Wiart, C., Gomes, G., Russo, C., Decremer, D., Grimaldi, S., Disperati, J., Ziese, M., Schweim, C., Garcia Sanchez, R., Jacobson, T., Ramos, A., Prudhomme, C., and Salamon, P.: EFAS v5.0 hydrological reanalysis, JRC Technical Report JRC134686, European Commission, Joint Research Centre (JRC), Ispra, Italy, 2023.

MEDOC Group: Observation of formation of deep water in the Mediterranean Sea, 1969, Nature, 227, 1037–1040, https://doi.org/10.1038/2271037a0, 1970.

Mellor, G. L. and Yamada, T.: Development of a turbulence closure model for geophysical fluid problems, Reviews of Geophysics, 20, 851–875, https://doi.org/10.1029/RG020i004p00851, 1982.

Millot, C. and Taupier-Letage, I.: Circulation in the Mediterranean Sea, in: The Mediterranean Sea, pp. 29–66, Springer, 2005.

Murphy, A. H.: Skill scores based on the mean square error and their relationships to the correlation coefficient, Monthly Weather Review, 116, 2417–2424, https://doi.org/10.1175/1520-0493(1988)116<2417:SSBOTM>2.0.CO;2, 1988.

Murphy, A. H.: Climatology, persistence, and their linear combination as standards of reference in skill scores, Weather and Forecasting, 7, 692–698, https://doi.org/10.1175/1520-0434(1992)007<0692:CPATLC>2.0.CO;2, 1992.

Oddo, P., Falchetti, S., Viola, S., Pennucci, G., Storto, A., Borrione, I., Giorli, G., Cozzani, E., Russo, A., Tollefsen, C.: Evaluation of different Maritime rapid environmental assessment procedures with a focus on acoustic performance, *The Journal of the Acoustical Society of America,* 152, 5, 2962–2981, 2022.

Oddo, P., Adani, M., Pinardi, N., Fratianni, C., Tonani, M., and Pettenuzzo, D.: A nested Atlantic–Mediterranean Sea general circulation model for operational forecasting, Ocean Science, 5, 461–473, https://doi.org/10.5194/os-5-461-2009, 2009.

Oke, P. R., Allen, J. S., Miller, R. N., Egbert, G. D., Austin, J. A., Barth, J. A., Boyd, T. J., Kosro, P. M., and Levine, M. D.: A modeling study of the three-dimensional continental shelf circulation off Oregon. Part I: Model-data comparison, Journal of Physical Oceanography, 32, 1360–1382, https://doi.org/10.1175/1520-0485(2002)032<1360:AMOSOT>2.0.CO;2, 2002.

Pacanowski, R. and Philander, S.: Parameterization of vertical mixing in numerical models of tropical oceans, Journal of Physical Oceanog- raphy, 11, 1443–1451, 1981.

Pinardi, N. and Masetti, E.: Variability of the large scale general circulation of the Mediterranean Sea from observations and modelling: A review, Palaeogeography, Palaeoclimatology, Palaeoecology, 158, 153–173, https://doi.org/10.1016/S0031-0182(00)00048-1, 2000.

Pinardi, N., Masetti, P., and Navarra, G.: Mediterranean Sea general circulation: A coupled modeling study, Journal of Geophysical Research, 108, 3149, https://doi.org/10.1029/2002JC001542, 2003.

Pinardi, N., Bregant, R., and Masetti, P.: The Atlantic–Ionian–Eastern Mediterranean (AIM) dynamic system, Dynamics of Atmospheres and Oceans, 37, 231–252, https://doi.org/10.1016/j.dynatmoce.2004.04.002, 2004.

Pinardi, N., Estournel, C., Cessi, P., Escudier, R. and Lyubartsev, V., Dense and deep water formation processes and Mediterranean overturning circulation. In *Oceanography of the mediterranean sea* (pp. 209-261). Elsevier, 2023.

Poulain, P.-M., Barbanti, R., Font, J., Cruzado, A., Millot, C., Gertman, I., Griffa, A., Molcard, A., Rupolo, V., Le Bras, S., et al.: MedArgo: a drifting profiler program in the Mediterranean Sea, Ocean Science, 3, 379–395, 2007.

Rahmstorf, S.: A fast and complete convection scheme for ocean models, Ocean Modelling, 101, 9–11, 1993.
Reffray, G., Bourdallé-Badie, R., and Calone, C.: Modelling turbulent vertical mixing sensitivity using a 1-D version of NEMO, Geoscientific Model Development, 8, 69–86, https://doi.org/10.5194/gmd-8-69-2015, 2015.

Rascle, N., Ardhuin, F., Queffeulou, P., & Croizé-Fillon, D., A global wave parameter database for geophysical applications. Part 1: Wave-current–turbulence interaction parameters for the open ocean based on traditional parameterizations, Ocean Modelling, 25, 3-4, 154-171, 2008.

Robertson, R.: An evaluation of the performance of vertical mixing parameterizations for tidal mixing in the Regional Ocean Modeling System (ROMS), Geoscience Letters, 6, 15, https://doi.org/10.1186/s40562-019-0146-y, 2019.

Robinson, A. R. and Golnaraghi, M. F.: Levantine Intermediate Water spreading in the eastern Mediterranean Sea: Comparison of numerical simulations and observations, Journal of Geophysical Research, 98, 10 023–10 038, https://doi.org/10.1029/93JC00257, 1993.

Roether, W., Klein, A., Spall, M., and Rhein, M.: Deep Water Formation in the Eastern Mediterranean, Journal of Geophysical Research, 101, 8975–8989, https://doi.org/10.1029/95JC03851, 1996.

Said, M. A., Gerges, M. A., Maiyza, I. A., Hussein, M. A., and Radwan, A. A.: Changes in Atlantic Water characteristics in the south-eastern Mediterranean Sea as a result of natural and anthropogenic activities, Oceanologia, 53, 81–95, https://doi.org/10.5697/oc.53-1.81, 2011.

Schroeder, K., Somot, M., Estournel, C., Sevault, G., and Desportes, E.: Abrupt climate shift in the Western Mediterranean Sea, Scientific Reports, 2, https://doi.org/10.1038/srep00946, 2012.

Send, U., Font, J., and Pujol, M.: Recent advances in understanding deep water formation in the northwestern Mediterranean, Journal of Marine Systems, 7, 273–293, https://doi.org/10.1016/S0924-7963(96)00036-7, 1996.

Shchepetkin, A. F.: An adaptive, Courant-number-dependent implicit scheme for vertical advection in oceanic modeling, Ocean Modelling, 91, 38–69, 2015.

Simoncelli, S., Pinardi, N., Fratianni, C., Dubois, C., and Notarstefano, G.: Water mass formation processes in the Mediterranean Sea over the past 30 years. Copernicus Marine Service Ocean State Report, Issue 2. K. von Schuckmann et al., Eds., s96- s100, J. Oper. Oceanogr., 11, s1–s142, 2018.

Simoncelli, S., Sannino, S., Mazloff, M. R., Vetrano, A., and et al.: Mediterranean Ocean State Report 2, Tech. rep., Euro-Mediterranean Center on Climate Change (CMCC), https://med.oceanrep.org/, accessed: 2025-07-31, 2022.

Somot, S., Sevault, G., and Déqué, M.: Transitional climate change scenarios for the Mediterranean region, Climate Dynamics, 27, 851–879, https://doi.org/10.1007/s00382-006-0126-6, 2006.

Storto, A., Hesham Essa, Y., de Toma, V., Anav, A., Sannino, G., Santoleri, R., and Yang, C.: MESMAR v1: a new regional coupled climate model for downscaling, predictability, and data assimilation studies in the Mediterranean region, Geoscientific Model Development Discussions, 1–40, 2023.

Testor, P. and Mortier, L.: Modeling and observing the formation of deep water in the Northwestern Mediterranean Sea, Oceanography, 18, 56–67, 2005.

Testor, P., Mortier, L., Bosse, A., et al.: Multiscale observations of deep convection in the northwestern Mediterranean Sea during winter 2012–2013 using multiple platforms, Journal of Geophysical Research: Oceans, 123, 1745–1776, https://doi.org/10.1002/2016JC012671, 2018.

Theocharis, A., Lascaratos, A., Nittis, K., and Georgopoulos, D.: The intermediate waters of the Mediterranean Sea: a review, Progress in Oceanography, 55, 287–316, https://doi.org/10.1016/S0079-6611(02)00114-3, 2002.

Tolman, H. L.: User Manual and System Documentation of WAVEWATCH III^{TM} version 6.07, Tech. rep., NOAA/NWS/NCEP/MMAB, https: //polar.ncep.noaa.gov/waves/wavewatch/wavewatch.shtml, 2021.

Tonani, M., Pinardi, N., Fratianni, C., Pistoia, J., Dobricic, S., Pensieri, S., de Alfonso, M., and Nittis, K.: Mediterranean Forecasting System: forecast and analysis assessment through skill scores, Ocean Science, 5, 649–660, https://doi.org/10.5194/os-5-649-2009, 2009.

Umlauf, L. and Burchard, H.: A generic length-scale equation for geophysical turbulence models, Journal of Marine Research, 61, 235–265, https://doi.org/10.1357/002224003322005087, 2003.

Villarreal, M.R., K. Bolding, Burchard, H., and E. Demirov, Coupling of the GOTM turbulence module to some three-dimensional ocean models, pp. 225-237. In: Baumert, H.Z., J.H. Simpson, and J. Sündermann (eds.), Marine Turbulence: Theories, Observations and Models, Cambridge University Press, Cambridge, 630 pp. 2005.

Von Schuckmann, K., Le Traon, P.-Y., Smith, N., Pascual, A., Brasseur, P., Fennel, K., Djavidnia, S., Aaboe, S., Fanjul, E. A., Autret, E., et al.: Copernicus marine service ocean state report, Journal of Operational Oceanography, 11, S1–S142, 2018.

Wesson, J. C. and Gregg, M. C.: Mixing at Camarinal Sill in the Strait of Gibraltar, Journal of Geophysical Research: Oceans, 99, 9847–9878, https://doi.org/10.1029/94JC00256, 1994.

Willmott, C. J.: On the validation of models, Physical Geography, 2, 184–194, https://doi.org/10.1080/02723646.1981.10642213, 1981.

Wong, A. P., Wijffels, S. E., Riser, S. C., Pouliquen, S., Hosoda, S., Roemmich, D., Gilson, J., Johnson, G. C., Martini, K., Murphy, D. J., et al.: Argo data 1999–2019: Two million temperature-salinity profiles and subsurface velocity observations from a global array of profiling floats, Frontiers in Marine Science, 7, 700, 2020.